The Astrophysical Journal, 926:165 (17pp), 2022 February 20 https://doi.org/10.3847/1538-4357/ac3df8

ALMA Observations of NGC 6334S. II. Subsonic and Transonic Narrow Filaments in a High-mass Star Formation Cloud

Shanghuo Li[1], Patricio Sanhueza[2,3], Chang Won Lee[1,4], Qizhou Zhang[5], Henrik Beuther[6], Aina Palau[7], Hong-Li Liu[8], Howard A. Smith[5], Hauyu Baobab Liu[9], Izaskun Jiménez-Serra[10], Kee-Tae Kim[1,4], Siyi Feng[2,9,11], Tie Liu[12], Junzhi Wang[12], Di Li[11,13], Keping Qiu[14], Xing Lu[2,12], Josep Miquel Girart[15], Ke Wang[16], Fei Li[14], Juan Li[12], Yue Cao[5,14], Shinyoung Kim[1,4], and Shaye Strom[5]

[1] Korea Astronomy and Space Science Institute, 776 Daedeokdae-ro, Yuseong-gu, Daejeon 34055, Republic Of Korea; shanghuo.li@gmail.com
[2] National Astronomical Observatory of Japan, National Institutes of Natural Sciences, 2-21-1 Osawa, Mitaka, Tokyo 181-8588, Japan
[3] Department of Astronomical Science, SOKENDAI (The Graduate University for Advanced Studies), 2-21-1 Osawa, Mitaka, Tokyo 181-8588, Japan
[4] University of Science and Technology, 217 Gajeong-ro, Yuseong-gu, Daejeon 34113, Republic Of Korea
[5] Center for Astrophysics | Harvard & Smithsonian, 60 Garden Street, Cambridge, MA 02138, USA
[6] Max Planck Institute for Astronomy, Konigstuhl 17, D-69117 Heidelberg, Germany
[7] Instituto de Radioastronomía y Astrofísica, Universidad Nacional Autónoma de México, P.O. Box 3-72, 58090, Morelia, Michoacán, México
[8] Department of Astronomy, Yunnan University, Kunming, 650091, People's Republic of China
[9] Academia Sinica Institute of Astronomy and Astrophysics, 11F of AS/NTU Astronomy-Mathematics Building, No.1, Section 4, Roosevelt Road, Taipei 10617, Taiwan
[10] Centro de Astrobiología (CSIC-INTA), Carretera de Ajalvir, Km. 4, Torrejón de Ardoz, E-28850 Madrid, Spain
[11] National Astronomical Observatories, Chinese Academy of Sciences, Beijing 100101, People's Republic of China
[12] Shanghai Astronomical Observatory, Chinese Academy of Sciences, 80 Nandan Road, Shanghai 200030, People's Republic of China
[13] NAOC-UKZN Computational Astrophysics Centre, University of KwaZulu-Natal, Durban 4000, South Africa
[14] School of Astronomy and Space Science, Nanjing University, 163 Xianlin Avenue, Nanjing 210023, People's Republic of China
[15] Institut de Ciències de l'Espai (IEEC-CSIC), Campus UAB, Carrer de Can Magrans s/n, E-08193 Cerdanyola del Vallès, Catalonia, Spain
[16] Kavli Institute for Astronomy and Astrophysics, Peking University, 5 Yiheyuan Road, Haidian District, Beijing 100871, People's Republic of China
Received 2021 August 18; revised 2021 November 1; accepted 2021 November 23; published 2022 February 22

Abstract

We present a study of narrow filaments toward a massive infrared dark cloud, NGC 6334S, using the Atacama Large Millimeter/submillimeter Array. Thirteen gas filaments are identified using the $H^{13}CO^+$ line, while a single continuum filament is revealed by the continuum emission. The filaments present a compact radial distribution with a median filament width of ∼0.04 pc, narrower than the previously proposed "quasi-universal" 0.1 pc filament width. The higher spatial resolution observations and higher density gas tracer tend to identify even narrower and lower mass filaments. The filament widths are roughly twice the size of embedded cores. The gas filaments are largely supported by thermal motions. The nonthermal motions are predominantly subsonic and transonic in both identified gas filaments and embedded cores, which may imply that stars are likely born in environments of low turbulence. A fraction of embedded objects show a narrower velocity dispersion compared with their corresponding natal filaments, which may indicate that turbulent dissipation is taking place in these embedded cores. The physical properties (mass, mass per unit length, gas kinematics, and width) of gas filaments are analogous to those of narrow filaments found in low- to high-mass star-forming regions. The more evolved sources are found to be farther away from the filaments, a situation that may have resulted from the relative motions between the young stellar objects and their natal filaments.

Unified Astronomy Thesaurus concepts: Protoclusters (1297); Interstellar medium (847); Interstellar line emission (844); Star formation (1569); Star forming regions (1565); Early-type stars (430); Infrared dark clouds (787)

Supporting material: figure set

1. Introduction

Filamentary structures of the interstellar medium (ISM) are prevalent in nearby Gould Belt molecular clouds and also more distant molecular clouds as seen in recent Galactic plane surveys from far-infrared to centimeter wavelengths and in both continuum and molecular line emission (Churchwell et al. 2009; André et al. 2010; Molinari et al. 2010; Arzoumanian et al. 2011; Goodman et al. 2014; Wang et al. 2015; Zucker et al. 2015; Contreras et al. 2016; Li et al. 2016; Soler et al. 2020; Wang et al. 2020). These filaments show wide ranges of physical properties (e.g., length, width, mass, length-to-width aspect ratios, and mass per unit length) that can vary over an order of magnitude across the revealed filaments.

Similar filamentary structures are also commonly seen in both numerical hydrodynamic and magnetohydrodynamic simulations of the ISM (e.g., Padoan et al. 2007; Heitsch et al. 2008; Gong & Ostriker 2011; Hennebelle 2013; Gómez & Vázquez-Semadeni 2014). Several mechanisms have been proposed for the formation of filaments in molecular clouds, such as gravitational instability (gravitational fragmentation and collapse) of sheet-like and elongated clouds (Miyama et al. 1987; Nagai et al. 1998; Hartmann & Burkert 2007; Hennebelle 2013; Gómez & Vázquez-Semadeni 2014; Van Loo et al. 2014), cloud collision (Padoan et al. 2001), and shocked flows (Gong & Ostriker 2011; Chen et al. 2020).

In dense and self-gravitating clouds, filaments often exhibit cylindrical morphologies (e.g., Taurus B213; Li & Goldsmith 2012).

Large-scale filaments often harbor parsec-scale dense massive clumps that become the fertile ground of massive star and cluster formation (Zhang et al. 2009; Jiménez-Serra et al. 2014; Wang et al. 2014; Busquet et al. 2016), although not all filaments show signs of star formation activity (e.g., only prestellar cores are detected in the Polaris flare; Miville-Deschênes et al. 2010). The embedded dense cores that are precursors of stars can be formed in the highest density regions of the filament via contraction by self-gravity and local kinematic processes (Inutsuka & Miyama 1992; Hartmann & Burkert 2007; Heitsch et al. 2008, 2009; Nakamura & Li 2008; Myers 2009; Gong & Ostriker 2011). The prestellar cores and protostellar cores are primarily found to reside in dense filamentary structures with supercritical masses per unit length in both low- and high-mass star-forming molecular clouds (André et al. 2014; Chung et al. 2019; Treviño-Morales et al. 2019), and most of them are believed to have formed by cloud collapse and/or fragmentation along filaments (Men'shchikov et al. 2010; André et al. 2014; Henshaw et al. 2014; Peretto et al. 2014; Beuther et al. 2015; Könyves et al. 2015; Clarke et al. 2017). The gas flows along filaments can continuously supply the material for cores to grow in mass (Liu et al. 2012; Kirk et al. 2013; Lin et al. 2017; Lu et al. 2018; Yuan et al. 2018; Liu et al. 2019; Treviño-Morales et al. 2019; Sanhueza et al. 2021).

Recently, Atacama Large Millimeter/submillimeter Array (ALMA) high angular resolution observations reveal that narrow (i.e., filament widths of a few times 0.01 pc) filamentary structures (or "fibers" in Hacar et al. 2018) are found in some high-mass star-forming clouds (e.g., Orion, G035.39–00.33, and G14.225–0.506; Henshaw et al. 2014; Hacar et al. 2018; Monsch et al. 2018; Chen et al. 2019b, and references therein). These filaments are much narrower than the "quasi-universal" 0.1 pc filament width proposed by previous studies using Herschel observations (e.g., André et al. 2014; Arzoumanian et al. 2019, and references therein), and appear to be intimately linked to dense cores (Hacar et al. 2018). However, whether such narrow filamentary structures are ubiquitous in high-mass star formation clouds and what their properties are remain controversial topics to be more fully explored.

To understand the nature of filaments and embedded dense cores in massive star formation regions, we have carried out high angular resolution observations toward a filamentary infrared dark cloud, NGC 6334S, using the ALMA. NGC 6334S is located at the southwestern end of the NGC 6334 molecular cloud complex (Figure 1), which is a nearby (1.3 kpc) young and massive "mini-starburst" region (Chibueze et al. 2014; Willis et al. 2013). In contrast to the well-known infrared bright OB cluster-forming clumps NGC 6334I/I(N)/II/III/IV/V (Persi & Tapia 2008; Russeil et al. 2013), NGC 6334S in some areas is dark in the infrared at wavelengths up to 70 μm (see Figure 1 of Li et al. 2020a, hereafter Paper I), signaling its youth. NGC 6334S has a mass of $\sim$1390 $M_\odot$ (Paper I), which is comparable to the clumps with embedded massive protostars and protoclusters elsewhere in the complex, and therefore has the potential to form massive stars together with lower mass star clusters. Thus NGC 6334S provides an ideal laboratory in which to investigate the early evolutionary stages of cluster formation in filamentary clouds. We will use dense gas tracers and continuum emission not only to identify the filamentary structures in the position–position–velocity (PPV) space but also to study the physical properties (e.g., gas kinematics, mass, structure profile) of both filaments and dense cores in order to understand the initial cloud environment of filament-based cluster formation.

We recently identified 49 continuum dense cores (hereafter continuum cores, named respectively #1, #2, #3, ...) using our 3 mm continuum image (Paper I) and found 17 starless cores (hereafter NH_2D cores, namely M1, M2, M3, ...) using the NH_2D line emission (Li et al. 2021, hereafter Paper II). These NH_2D cores are associated neither with continuum cores nor with Class I/II young stellar objects (YSOs; Willis et al. 2013). For simplicity, we refer to continuum cores and NH_2D cores as dense cores. The derived masses of dense cores range from 0.13 to 14.1 $M_\odot$, with the mean and median values of 1.8 and 0.8 $M_\odot$, respectively. The sizes of dense cores are between 0.01 and 0.04 pc, with the mean and median values of 0.018 and 0.017 pc, respectively. Paper I also shows that the nonthermal motions are predominantly subsonic and transonic throughout NGC 6334S and that the external pressure is important in confining the embedded objects. Paper II reported the presence of a cluster of low-mass starless and prestellar cores that show small velocity dispersions, a high fractional abundance of NH_2D, and high NH_3 deuterium fractionation, and that are dark at infrared wavelengths to 70 μm. In at least some of the NH_2D cores, turbulence seems dissipated and the gas kinematics is dominated by thermal motions.

In this work, we focus on filaments and investigate their properties as well as the relationship between filaments and dense cores. The observations are described in Section 2. Then, we describe the filament identification and the properties of identified filaments in Section 3. We discuss in detail the properties of filaments and dense objects in Section 4. Finally, we summarize our main findings in Section 5.

2. Observation

We have carried out a 55 pointing mosaic observation with the ALMA 12 m array toward the massive infrared dark cloud (IRDC) NGC 6334S between 2017 March 13 and 21 (ID: 2016.1.00951.S). Two 234.4 MHz wide spectral windows were employed to cover the $H^{13}CO^+$ (1–0, 86.7 GHz) and NH_2D ($1_{1,1}-1_{0,1}$, 85.9 GHz) lines with a 0.061 MHz spectral resolution ($\sim$0.21 km s^{-1} at 86 GHz). In addition, three 1.875 GHz wide spectral windows centered at 88.5 GHz, 98.5 GHz, and 100.3 GHz with a spectral resolution of 0.977 MHz ($\sim$3.0–3.3 km s^{-1}) were used to take broadband continuum data. More details of the observations can be found in Paper I.

Data calibration was performed using the CASA 4.7.0 software package (McMullin et al. 2007). Both continuum and line images were iteratively cleaned with manual masking via the *clean* task down to $\sim3\sigma$ using the multiscale deconvolver and a robust weighting of 0.5. The resultant continuum and line images have a synthesized beam of $\theta_{\rm maj} \times \theta_{\rm min} = 3\farcs6 \times 2\farcs4$ (or 0.023 pc $\times$ 0.015 pc, with a position angle P.A. = 81°) and $\theta_{\rm maj} \times \theta_{\rm min} = 4\farcs1 \times 2\farcs8$ (or 0.026 pc $\times$ 0.018 pc, P.A = 83°), respectively. The achieved 1σ rms noise levels are 0.3 mJy beam^{-1} for the continuum image and $\sim$6 mJy beam^{-1} per 0.21 km s^{-1} for the spectral line images. The maximum recoverable scale of a single pointing reaches up to $\sim30''$ in the ALMA data. All images shown in this paper are prior to primary beam correction. The measured fluxes for mass estimation have the primary beam correction applied.

3. Results and Analysis

NGC 6334S is mostly dark at infrared wavelengths to 70 μm, indicating its early evolutionary stage (e.g.,

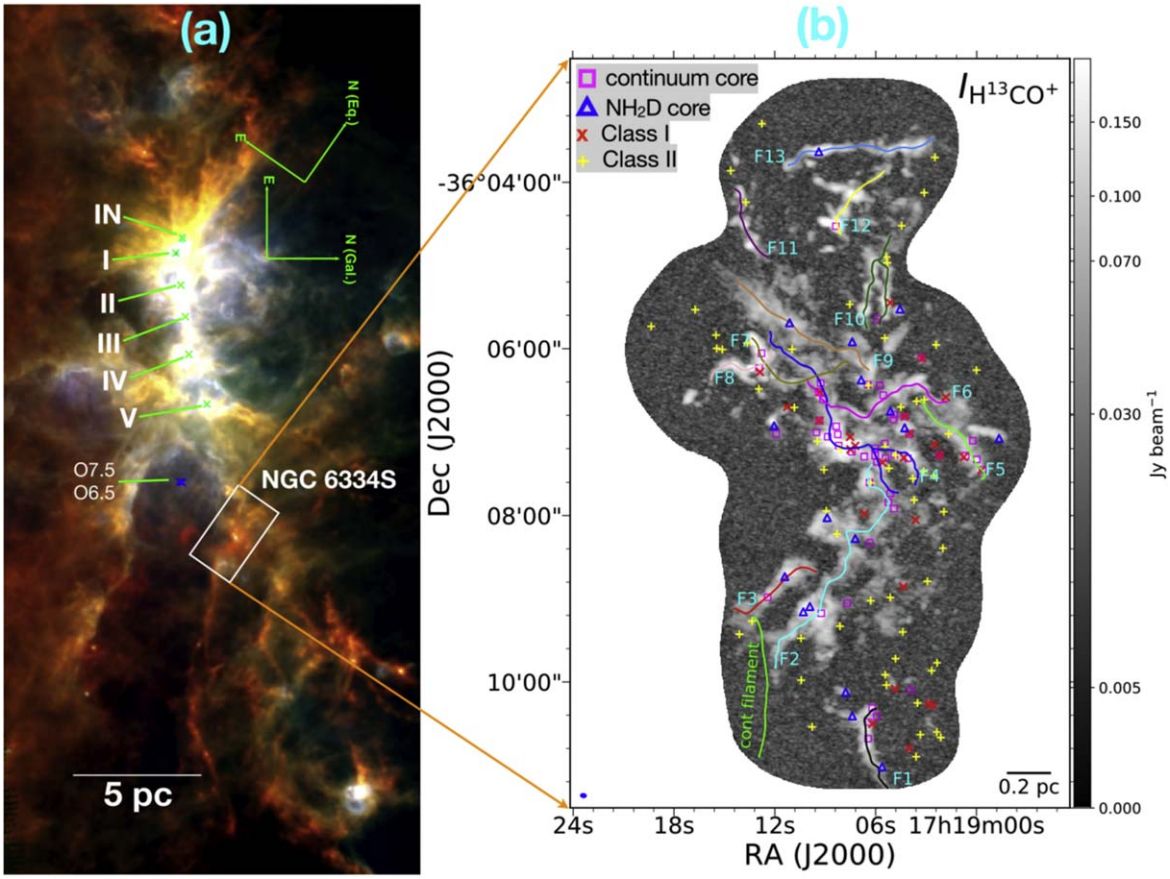

Figure 1. Panel (a): three-color Herschel composite image of NGC 6334 molecular cloud complex with blue, green, and red for $\lambda = 70$, 160, and 350 μm, respectively. The scale bar (5 pc at the distance of 1.3 kpc) and the Equatorial and the Galactic cardinal directions are shown on the upper right side of the image. The white box presents the NGC 6334S region. Six bright infrared (IR) clumps (I, IN, II, III, IV, and V) are marked in the image (McBreen et al. 1979). Two O type stars (O7.5 and O6.5) are marked with blue cross "×" symbols (Persi & Tapia 2008). Panel (b): the filament spines (color solid curves) overlaid on the peak intensity ($I_{H^{13}CO^+}$; the maximum intensity of the spectrum) image of $H^{13}CO^+$ line emission. Magenta open squares correspond to the 49 continuum cores identified by the ALMA 3mm continuum image (Paper I). Blue open triangles show the 17 NH_2D cores revealed by the NH_2D line emission (Paper II). The red cross "×" and yellow plus "+" symbols correspond to the 25 Class I and 58 Class II young stellar objects (Willis et al. 2013), respectively. The beam size (blue filled ellipse) of the $H^{13}CO^+$ image is shown in the bottom left of the panel.

Sanhueza et al. 2013, 2019; Tan et al. 2013; Sanhueza et al. 2017; Contreras et al. 2018; Li et al. 2019a; Morii et al. 2021). Figure 1 shows an overview of the NGC 6334 molecular cloud complex in the far-infrared and the location of NGC 6334S.

3.1. Molecular Line Emission

The rotational transitions of several molecular species (i.e., HCO^+ (1–0), HCN (1–0), CS (2–1), HNCO ($4_{0,4}-3_{0,3}$), $H^{15}NC$ (1–0), CH_3OH ($5_{1,4}-4_{1,3}$), SO (2_2-1_1), and HC_3N (11–10)) were detected with a coarse spectral resolution of 0.977 MHz (or ∼3.0–3.3 km s^{-1}). However, with these low spectral resolution data we are not able to determine the kinematic properties of the molecular gas. Therefore, only the high spectral resolution (0.061 MHz ∼ 0.21 km s^{-1}) data of the $H^{13}CO^+$ (1–0) and NH_2D ($1_{1,1}-1_{0,1}$) lines will be used as diagnostics of the kinematic properties of the filaments in this work.

Figures 1 and 2 show the $H^{13}CO^+$ line, continuum, and NH_2D line emission. The $H^{13}CO^+$ (1–0; critical density $n_{cr} \sim 10^5$ cm^{-3}) line traces much more spatially extended gaseous structures than the NH_2D ($1_{1,1}-1_{0,1}$; $n_{cr} \sim 10^6$ cm^{-3}) line since their critical densities are different by nearly an order of magnitude. The NH_2D emission appears preferentially toward the location of dense cores. In addition, the $H^{13}CO^+$ emission is in better agreement with the Spitzer dark and Herschel bright filamentary structures than that of NH_2D (see also Paper I). These all suggest that the $H^{13}CO^+$ emission is a better tracer of filamentary structures than NH_2D. In what follows, $H^{13}CO^+$ will be therefore used to identify the velocity-coherent filamentary structures. There is the continuum filamentary structure in the southeastern part of the map (see Figures 1 and 2), of which the continuum emission is unlikely to be dominated by dust emission (see discussions below in Section 4.1).

We use the ∼7″ resolution NH_3 rotational temperatures (T_{NH_3}) derived in Paper I. For the regions where the NH_3 data are not available, we assume a gas kinematic temperature of $\langle T_{NH_3} \rangle = 15$ K, the average gas temperature derived from the observed NH_3 data.

3.2. Velocity Structures

Paper I found that multiple velocity components were detected in some areas where significant $H^{13}CO^+$ emission was detected. Since the majority (∼85%) of $H^{13}CO^+$ emission appears as a single velocity component, we show the intensity-weighted velocity (first moment) and intensity-weighted dispersion (second moment) of the $H^{13}CO^+$ line emission in

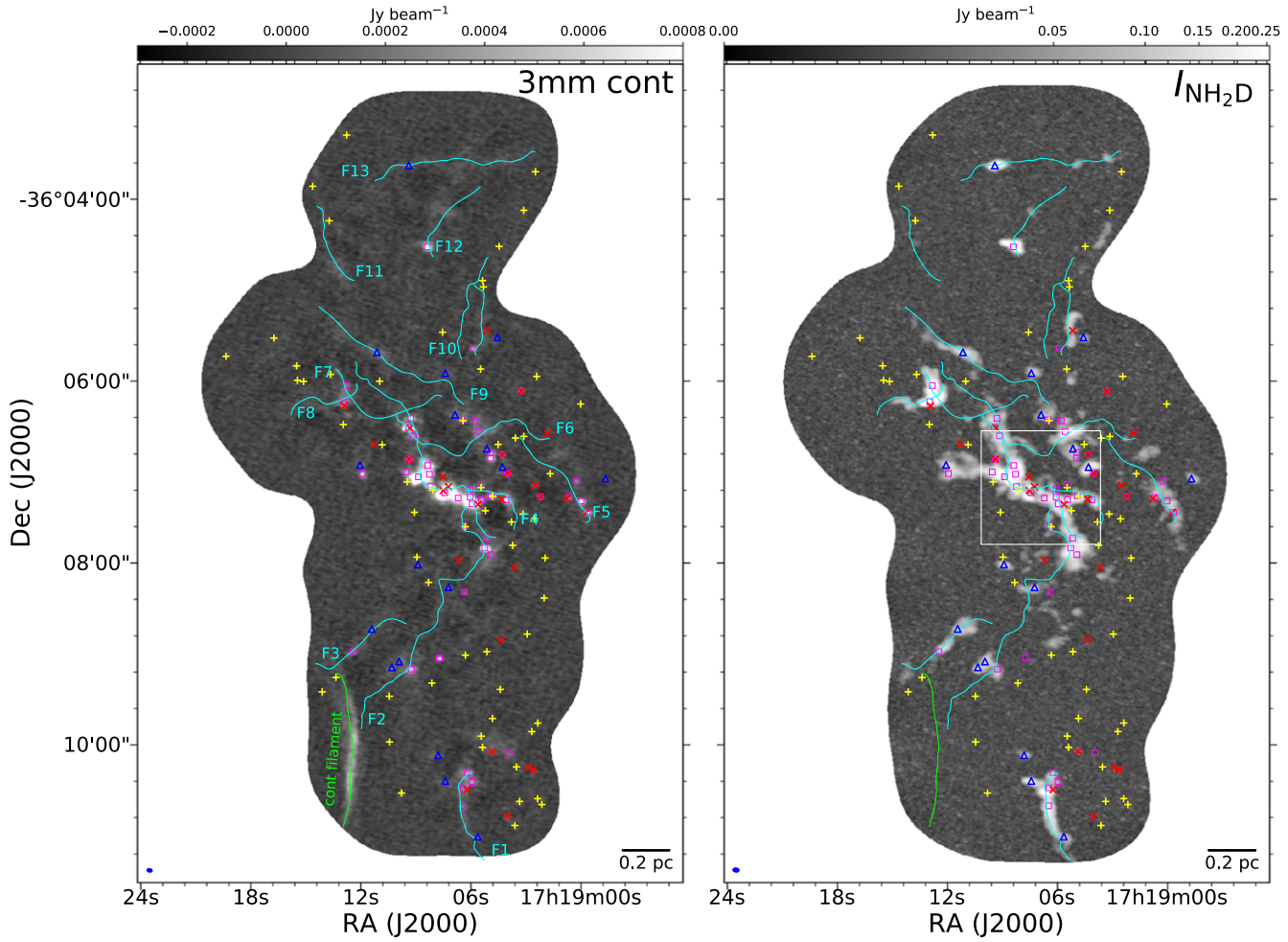

Figure 2. Magenta open squares, blue open triangles, red cross "×", and yellow plus "+" symbols show the continuum cores, NH_2D cores, Class I, and Class II objects, respectively. Left: the filament spines (cyan and green solid curves) overlaid on the 3 mm continuum image. Right: the filament spines (cyan and green solid curves) overlaid on the peak intensity map (I_{NH_2D}) of the NH_2D line emission. The white box shows the region where outflows are identified, with zoomed-in views presented in Section 4.2. The beam size is shown in the bottom left of each panel.

Figure 3. We note that there are complex velocity structures across NGC 6334S, especially toward the central region, which appears to be associated with multiple velocity components.

We fit Gaussian line profiles to the $H^{13}CO^+$ data pixel by pixel with multiple velocity components, under the assumption that the $H^{13}CO^+$ emission is optically thin. The detailed fitting process of molecular lines is summarized in Paper I. The observed velocity dispersions (σ_{obs}) derived from the Gaussian fitting are between 0.10 and 0.80 km s^{-1}, with mean and median values of 0.23 and 0.20 km s^{-1}, respectively. The observed σ_{obs} is composed of thermal and nonthermal components. Paper I shows that the nonthermal velocity dispersion σ_{nth} is dominated by subsonic and transonic motions throughout NGC 6334S. The σ_{obs} of the dense cores is greater than in the quiescent regions; the σ_{nth} and the σ_{obs} toward the central region of NGC 6334S have generally larger values than that measured in the outer regions (see Paper I).

3.3. Filament Identification

3.3.1. Friend-of-friend Algorithm

The results from the Gaussian fitting as described above in Section 3.2 were used to identify gas filaments. Following similar procedures as in Hacar et al. (2013, 2018), we use the Python-based friend-of-friend (fof) algorithm[17] (Huchra & Geller 1982) to identify the velocity-coherent filaments, i.e., those with no abrupt change of sign of the gradient along the filament in PPV space.

We first use the fof algorithm to identify the seed points, those that have peak intensities (I, the maximum intensity of the spectrum) above a certain threshold I_0 (7σ) of each individual structure. In total, about ∼70% of the data points are above I_0. The spatial criterion between nearby points for them to be considered as friends is $\Delta r \leqslant 0.023$ pc (∼1 beam size linear scale), while the velocity criterion uses an adaptive velocity gradient $\nabla v_{LSR,i} = \frac{1}{2}\frac{\triangle v_i}{\theta_{FWHM}}$ similar to the definition in Hacar et al. (2018). Here, $\triangle v_i$ is the line FWHM of $H^{13}CO^+$ of the ith pixel and θ_{FWHM} is the beam size. Only structures that contain more than 150 data points (the area of a structure larger than three times the beam size) were considered. Second, we run fof again to search for new friend points of each group identified in the first step, where the new friend points come from the remaining data points, in which the low intensity points ($\leqslant I_0$) are encompassed; the same spatial and velocity criteria are used. After the second fof run, there are about 20% of points that are not included within any group. The majority

[17] https://github.com/ShanghuoLi/pyfof

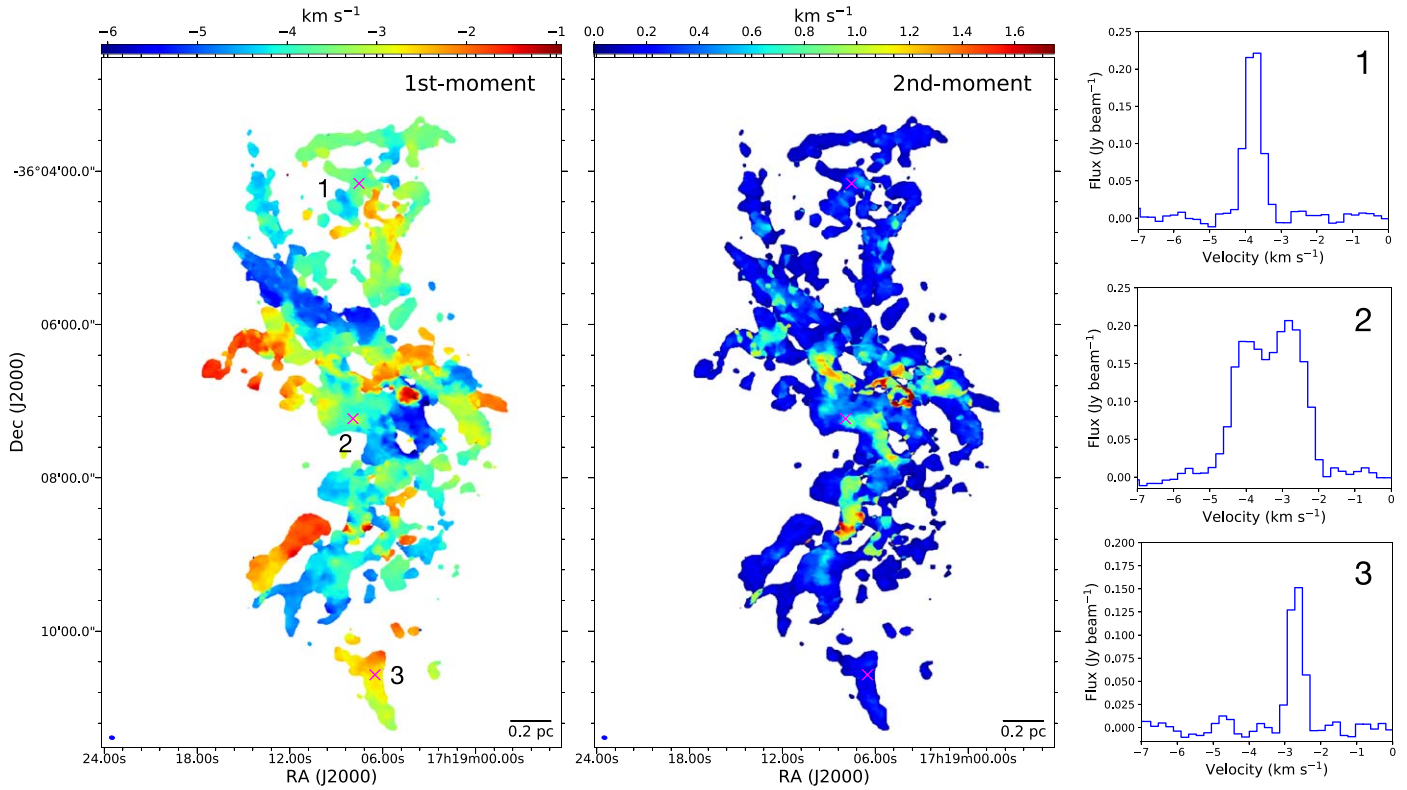

Figure 3. The left and middle panels show the $H^{13}CO^+$ intensity-weighted velocity (first moment) and intensity-weighted dispersion (second moment) maps, respectively. The beam size is shown in the bottom left of each panel. The right panel shows the spectra of $H^{13}CO^+$ extracted from positions 1, 2, and 3. Three selected positions are marked with a red cross "×" in both the left and middle panels.

of them have relatively low intensities and/or appear to be unaffiliated with the identified filaments.

We employ the `FilFinder`[18] algorithm to compute the filament spine. The `FilFinder` package reduces the masking area to identify a skeleton that represents the topology of the area, using a Medial Axis Transform. The masking area is delineated by the spatial distribution of the identified filaments; we refer to the derived skeletons as the filament spines. The derived filament spines are shown in Figure 1. In total, 13 velocity-coherent filaments have been identified by the fof algorithm from the PPV space of $H^{13}CO^+$ data. Filaments are named F1, F2, F3, ... in order from south to north. Filaments F4 and F10 have additional branches and they are named as F4b and F10b. The physical lengths of these identified filaments ($L_{\rm fil}$) range between 0.3 and 1.3 pc.

3.3.2. Velocity-coherent Filaments

The filament spines overlaid on the channel maps of $H^{13}CO^+$ are shown in Figure 4, which shows that the line emission exhibits a filamentary distribution and that the identified filaments are consistent with the majority of the $H^{13}CO^+$ emission. This provides further evidence that the Python-based fof algorithm can accurately recover the gas filamentary structures that are connected in both velocity and space (see also Figure 5).

Several small regions show significant $H^{13}CO^+$ emission but are not grouped into any identified filament. For instance, there is a small $H^{13}CO^+$ emission region on the west of F2 at a velocity range of between −4.20 and −3.78 km s^{-1}, which is marked with red arrows in Figure 4. Two separated substructures appear in this small region, implying the emission is not connected in the spatial space. There are also some isolated small regions separated from the identified filaments in spatial space. These isolated regions fail to be considered as an independent filament because their emission is too weak and/or the number of total data points is lower than the criteria used for identification. We stress that the identified filaments are likely to be incomplete. Potential low density and diffuse molecular filamentary structures could have been missed if their $H^{13}CO^+$ line emission is not significant and/or the detection suffers from severe missing flux.

The $H^{13}CO^+$ line emission of identified filaments generally spans $\geqslant$4 channels (a velocity range of $\geqslant$0.84 km s^{-1}). The filament with the largest spread in velocity is F4, which spans from −6.52 to −2.3 km s^{-1}. The majority of the filaments are spatially distinct, while several filaments partly overlap in position, such as F2–F4, F4–F6, F4–F7, and F7–F8. The overlapping regions tend to show complex velocity structures characterized by multiple velocity components along the line of sight.

3.4. Filament Profile

We employ the `RadFil`[19] package (Zucker & Chen 2018), a radial density profile building and fitting tool for interstellar filaments, to construct the filament radial profile from the velocity-integrated intensity of $H^{13}CO^+$ inside the mask of a given filament. We use the `RadFil` tangent to the filament spine at 7 or 8 pixel (about 1 beam size; 1 pixel = 0.″43) intervals along the filament, then we take the radial cut perpendicular to each tangent.

[18] https://github.com/e-koch/FilFinder

[19] https://github.com/catherinezucker/radfil

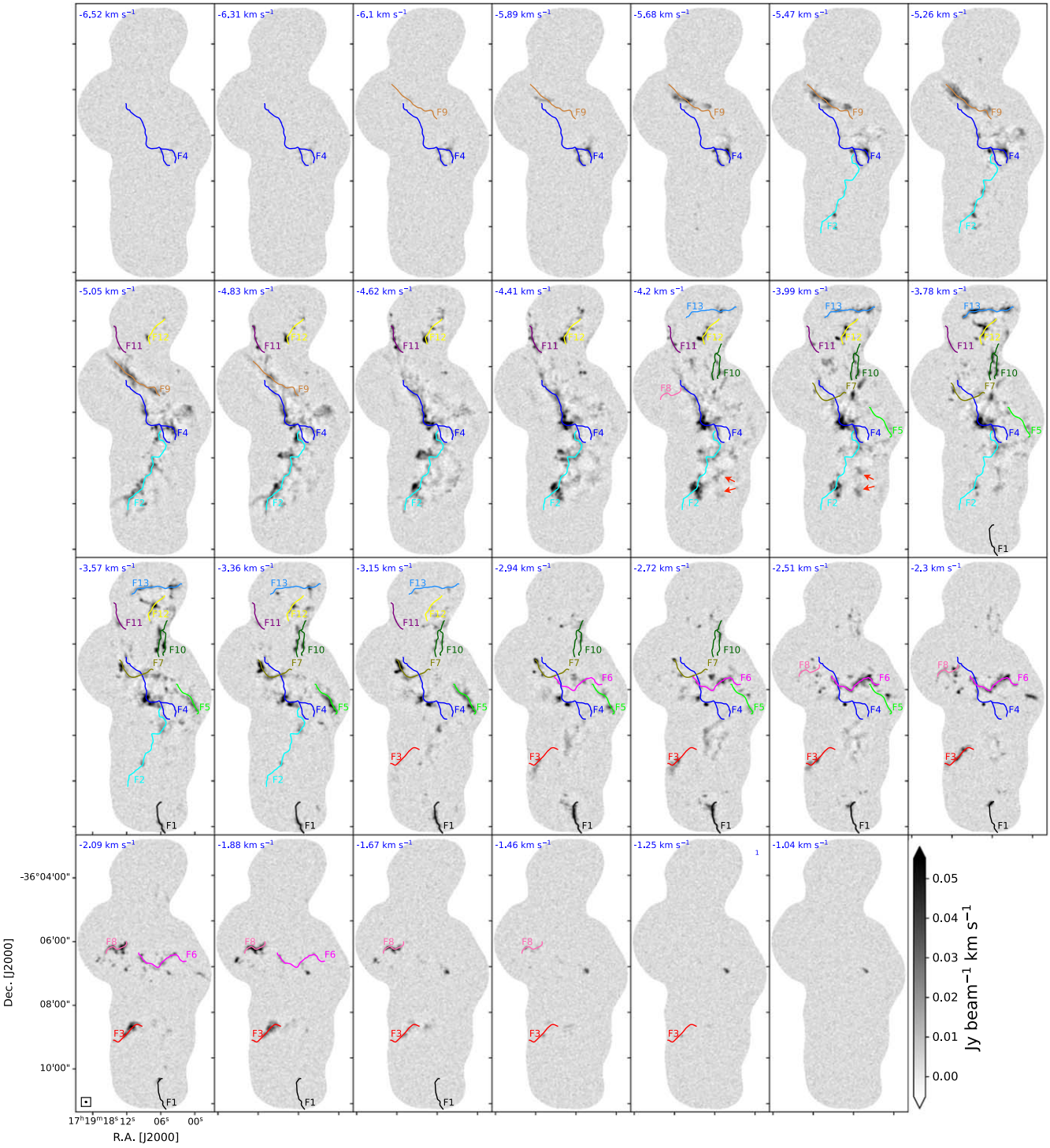

Figure 4. The filament spines (solid curves) overlaid on the channel map of $H^{13}CO^{+}$. The velocity value is presented in the top left of each panel.

The radial profile has been shifted along each cut in order to ensure that it is centered on the pixel with the peak intensity. Figure 6 shows the radial cut and the pixels (blue points) of the peak in the radial cut for F1. Along each cut, the radial distance is calculated as the projected distance from the peak intensity. Prior to fitting the profile, the background was subtracted using the background subtraction estimator of `RadFil`. The background is estimated by a first-order polynomial to all profiles at the given radial distance range, and then is subtracted from each cut; the background subtraction radii vary slightly from filament to filament, with a typical range of 0.08–0.15 pc.

To compute the filament widths (FWHM), we perform a Gaussian fitting to the average profile of the $H^{13}CO^{+}$ intensity of each filament. The Gaussian function is given by

$$A(r) = A_0 \exp\left(\frac{-(\mathrm{r} - \mu)^2}{2\sigma_{\mathrm{G}}^2}\right), \quad (1)$$

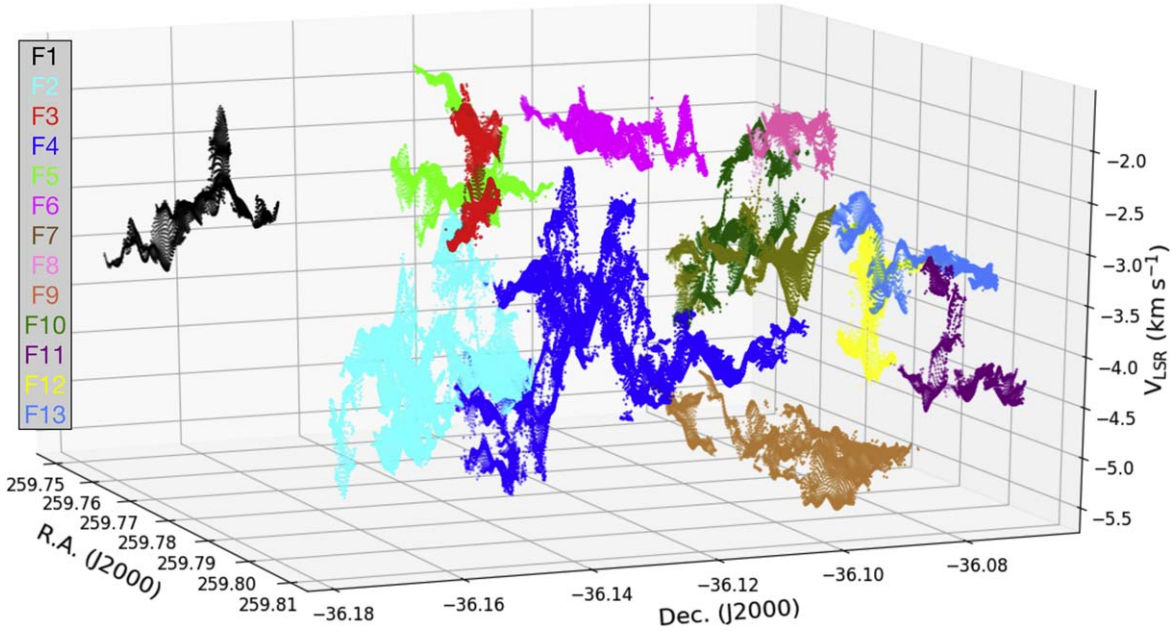

Figure 5. Position–position–velocity (PPV) cube shows the centroid velocity of the identified filaments. (The animated version of the PPV cube is available at https://github.com/ShanghuoLi/NGC6334S-filament.)

where r is the radial distance, A is the profile amplitude at the radial distance r, A_0 is the amplitude, σ_G is the standard deviation, and μ is the mean. Here, μ is fixed to zero. The best-fit Gaussian of each filament profile is listed in Table 1. An example of the fit is shown in Figure 6, where the red solid line is the best fit, the black dots correspond to the averaged integrated intensity of $H^{13}CO^+$, and the error bars are the standard deviation of the radial profile of all cuts perpendicular to the filament. The best-fit filament widths range from 0.036 to 0.074 pc, with the mean and median values of 0.046 and 0.045 pc, respectively. We also estimate the beam-deconvolved FWHM with $\mathrm{FWHM_{decon}} = \sqrt{\mathrm{FWHM}^2 - \mathrm{FWHM}_{\mathrm{bm}}^2}$, where $\mathrm{FWHM_{bm}}$ is the half-power beam width. The $\mathrm{FWHM_{bm}}$ is about 3.″4 (∼0.021 pc) in our observations. The $\mathrm{FWHM_{decon}}$ is between 0.029 and 0.071 pc, with the mean and median values of 0.041 and 0.039 pc, respectively.

In previous studies, observed filaments have been considered as cylindrical structures that can be described by a Plummer-like function of the form (e.g., Nutter et al. 2008; Arzoumanian et al. 2011; Palmeirim et al. 2013; Smith et al. 2014; Liu et al. 2018):

$$\int f dv(r) = \frac{A_0}{\left[1 + \left(\frac{r}{R_{\mathrm{flat}}}\right)^2\right]^{\frac{p-1}{2}}}, \quad (2)$$

where $\int f dv$ is the integrated intensity, A_0 is the peak profile amplitude, R_{flat} is the flattening radius, and p is the power-law index of the density profile at large radii (Cox et al. 2016; Zucker & Chen 2018). We also performed a Plummer fitting to the identified filaments in NGC 6334S. The best Plummer fit is shown as a dashed green line in Figure 6. The filament widths derived by the Plummer fitting are similar to those of the Gaussian fitting, and FWHM ranges from 0.03 to 0.066 pc, with the mean and median values of 0.045 and 0.042 pc, respectively. The $\mathrm{FWHM_{decon}}$ is between 0.023 and 0.062 pc, with the mean and median values of 0.039 and 0.037 pc (Table 1), respectively. R_{flat} is between 0.012 and 0.081 pc, with mean and median values of 0.033 and 0.027 pc, respectively. Figure 6 shows that some of the filament profiles have relatively large dispersions due to nonuniform line intensities throughout the filaments. The significant variations of $H^{13}CO^+$ emission across the filaments results in a poor fit in their profiles, e.g., F4 and F9.

The derived filament widths are similar to those of Musca (∼0.07 pc; Kainulainen et al. 2016), Aquila/Polaris (∼0.04 pc; Men'shchikov et al. 2010), Orion (∼0.02–0.05 pc for OMC-1/2 and ISF; Hacar et al. 2018), G14.225-0.506 (∼0.05–0.09 pc; Chen et al. 2019b), G035.39-00.33 (∼0.028 pc; Henshaw et al. 2017), and L1287 (∼0.03 pc; Sepúlveda et al. 2020). By contrast, the derived filament widths are narrower than those of Herschel filaments studied toward IC 5146 (∼0.1 pc; Arzoumanian et al. 2019), Taurus (∼0.1 pc; Palmeirim et al. 2013), NGC 6334IN, and NGC 6334I (∼0.24 pc; Russeil et al. 2013). But note that the spatial resolution of Herschel observations (beam size ∼36″) is much poorer than that of the ALMA observations. This supports the idea that higher spatial resolution observations and higher density gas tracers can identify narrower filaments. In addition, the dust continuum emission cannot be resolved into separate filaments when they overlap, whereas velocities measurements generally can. Spatially blended filaments might broaden the measured filament widths (see also Henshaw et al. 2017). This also indicates that filaments identified with different procedures might show deviating filament widths.

3.5. Filament Mass

The mass per unit length is one important indicator for assessing the stability of filaments. The continuum emission from dust is one of the most frequently used measurements to compute the mass. Figure 2 shows the filament spines overlaid on the 3 mm continuum image. Unfortunately, only two gas filaments (F4 and F1) have a significant continuum emission detection (Figure 2); the remaining 11 gas filaments are either only partly detected in continuum emission or not detected at

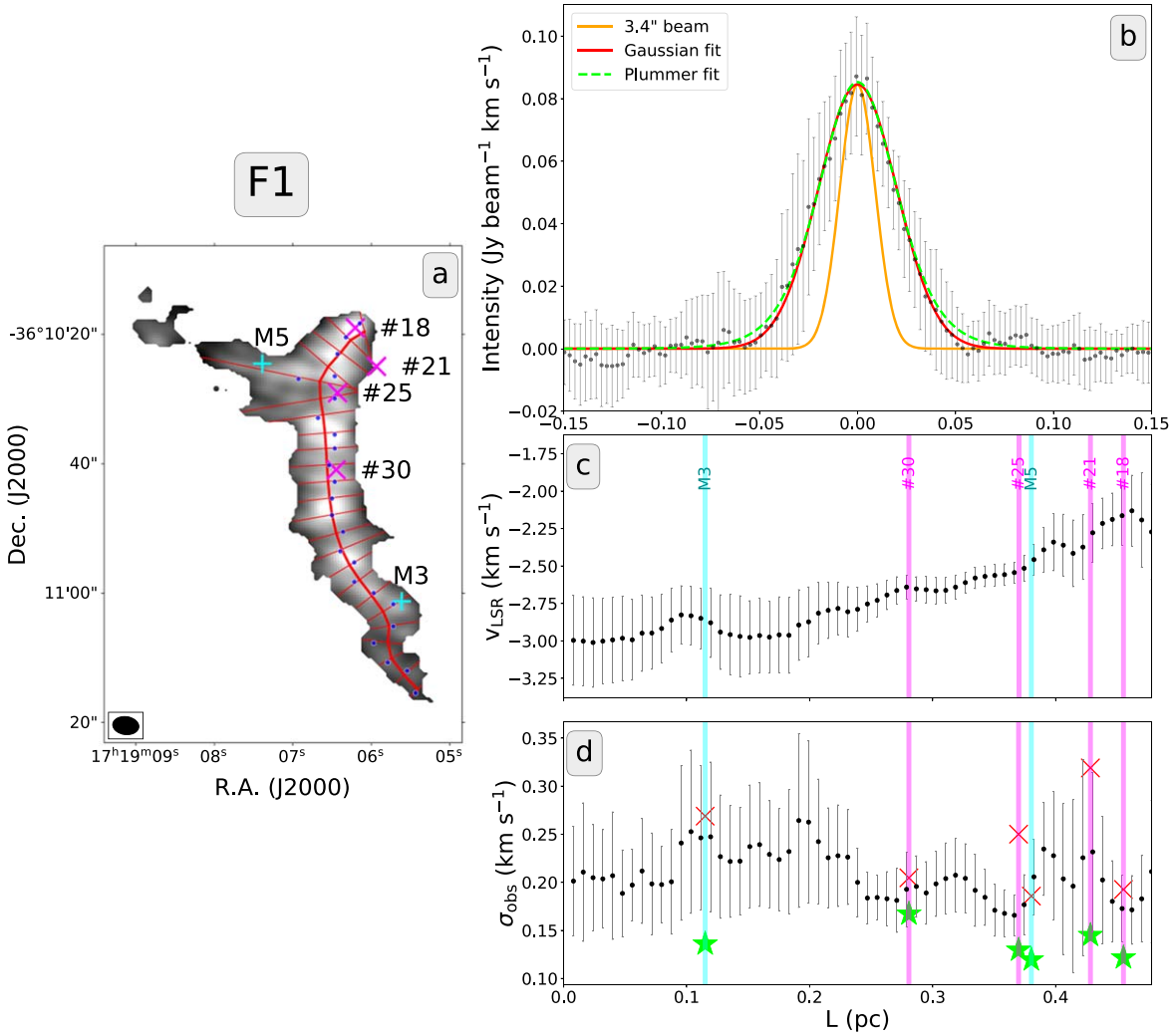

Figure 6. Panel (a): the filament spine (red solid curves) of F1 overlaid on the velocity-integrated intensity map of $H^{13}CO^+$. Magenta cross "×" and cyan plus "+" symbols are continuum cores and NH_2D cores, respectively. The beam size is shown in the bottom left of the panel. Panel (b): mean integrated intensity profile of $H^{13}CO^+$ (black dots) was built by sampling radial cuts (short red solid lines) every 8 pixels (which corresponds to 3.″44 or ∼0.019 pc at the source distance of 1.3 kpc) along the spine. The radial distance is the projected distance from the peak emission at a given cut (blue dots in panel (a)). The error bar represents the standard deviation of the cuts at each radial distance. The orange solid line shows the beam response with an FWHM of ∼3.″4. The red solid and green dashed lines present the best-fit results of Gaussian and Plummer fitting, respectively. Panels (c) and (d): the mean centroid velocity $\langle v_{\rm LSR}\rangle$ and mean observed velocity dispersion $\langle\sigma_{\rm obs}\rangle$ of $H^{13}CO^+$ line variation along the filament. The error bars show the standard deviations of the corresponding $v_{\rm LSR}$ and $\sigma_{\rm obs}$. Vertical magenta and cyan lines indicate the positions of associated continuum cores and NH_2D cores, respectively. The red cross "×" and green filled star symbols mark the core mean $\sigma_{\rm obs}$ derived from the $H^{13}CO^+$ and NH_2D lines, respectively.

(The complete figure set (15 images) is available.)

all above 5σ. An alternative way to estimate the filament mass is to make use of molecular gas emission; in this work we use $H^{13}CO^+$. With the fractional abundance of $H^{13}CO^+$ relative to H_2, $X(H^{13}CO^+) = N(H^{13}CO^+)/N(H_2)$, the filament mass can be computed as follows:

$$M_{\rm fil} = \mu_{\rm H_2}\, m_{\rm H} \sum \frac{N\,(H^{13}CO^+)}{X\,(H^{13}CO^+)}\,\Omega, \qquad (3)$$

where $N(H^{13}CO^+)$ is the column density of $H^{13}CO^+$, $\mu_{\rm H_2} = 2.8$ is the mean molecular weight of the ISM (Kauffmann et al. 2008), $m_{\rm H}$ is the hydrogen mass, and Ω is the solid angle of the $H^{13}CO^+$ emission. Assuming local thermodynamic equilibrium (LTE), the molecular column densities can be estimated from the velocity-integrated intensity (see Appendix A1), and finally lead to $M_{\rm fil}$ (see Equation (3)).

In order to estimate $X(H^{13}CO^+)$ for NGC 6334S, we have focused on F4 because both $H^{13}CO^+$ line and continuum emission are significantly detected (Figure 1 and 2). The derived $N(H^{13}CO^+)$ ranges from 7.2×10^{11} cm^{-2} to 1.4×10^{13} cm^{-2} and $N_{\rm H_2}$ is between 1.3×10^{22} cm^{-2} and 6.1×10^{23} cm^{-2}. The resulting values of $X(H^{13}CO^+)$ extend from 7.7×10^{-12} to 3.1×10^{-10}, with a median value of 5.4×10^{-11}. The derived $X(H^{13}CO^+)$ is similar to the reported values of 3.0×10^{-11}–4.0×10^{-10} in Butner et al. (1995), 4.5×10^{-11} in Gerner et al. (2014), 4.8×10^{-10} in Sanhueza et al. (2012), and 1.3×10^{-10} in Hoq et al. (2013).

Using the median $X(H^{13}CO^+) = 5.4\times10^{-11}$, we estimated the gas mass ($M_{\rm fil}$) for each filament. The derived masses are in the range of 4–82 $M_\odot$ (see Table 1) and the total gas mass in the filaments is about 342 $M_\odot$. The total gas mass estimated from $H^{13}CO^+$ in the observed region is about 395 $M_\odot$, which

Table 1
Physical Parameters of the Filaments

Filament	$L_{\rm fil}$	$M_{\rm fil}$	$M_{\rm line}$	$M_{\rm crit,tot}$	$M_{\rm crit,nth}$	$M_{\rm crit,th}$	Gaussian				Plummer				
							A_0 (10^{-2}	stddev	FWHM	$\rm FWHM_{decon}$	A_0 (10^{-2}	$R_{\rm flat}$	p	FWHM	$\rm FWHM_{decon}$
	(pc)	($M_\odot$)	($M_\odot$ pc^{-1})	($M_\odot$ pc^{-1})	($M_\odot$ pc^{-1})	($M_\odot$ pc^{-1})	Jy beam^{-1} km s^{-1})	(pc)	(pc)	(pc)	Jy beam^{-1} km s^{-1})	(pc)		(pc)	(pc)
(1)	(2)	(3)	(4)	(5)	(6)	(7)	(8)	(9)	(10)	(11)	(12)	(13)	(14)	(15)	(16)
F1	0.48	14	29	41	15	24	8.45 ± 0.12	0.020	0.047	0.042	8.53 ± 0.12	0.057 ± 0.009	9.78 ± 2.37	0.047	0.042
F2	1.37	52	38	47	20	24	5.20 ± 0.06	0.026	0.061	0.057	5.16 ± 0.14	0.081 ± 0.030	10.05 ± 5.74	0.066	0.062
F3	0.50	17	33	41	14	24	7.30 ± 0.11	0.023	0.054	0.049	7.25 ± 0.20	0.051 ± 0.012	6.27 ± 1.99	0.056	0.051
F4	1.27	82	64	65	36	25	8.39 ± 0.23	0.021	0.049	0.044	8.84 ± 0.26	0.021 ± 0.004	2.81 ± 0.34	0.045	0.039
F4b	0.27	4	14	41	15	24	9.90 ± 0.21	0.019	0.045	0.040	10.05 ± 0.29	0.014 ± 0.003	1.84 ± 0.17	0.057	0.053
F5	0.53	18	34	41	16	24	6.37 ± 0.16	0.024	0.056	0.052	6.73 ± 0.22	0.024 ± 0.004	2.78 ± 0.30	0.051	0.047
F6	0.86	16	19	43	14	24	5.06 ± 0.11	0.015	0.036	0.029	5.16 ± 0.15	0.023 ± 0.006	3.94 ± 1.08	0.036	0.029
F7	0.62	15	24	40	15	24	3.65 ± 0.18	0.016	0.037	0.030	3.77 ± 0.22	0.015 ± 0.006	2.40 ± 0.55	0.038	0.032
F8	0.40	11	28	42	18	24	7.46 ± 0.22	0.015	0.036	0.029	7.62 ± 0.19	0.034 ± 0.007	7.16 ± 2.05	0.034	0.027
F9	0.82	23	28	43	17	24	3.92 ± 0.13	0.031	0.074	0.071	4.29 ± 0.15	0.021 ± 0.005	2.17 ± 0.24	0.064	0.060
F10	0.53	13	26	44	19	24	8.34 ± 0.23	0.019	0.045	0.040	9.09 ± 0.25	0.014 ± 0.002	2.29 ± 0.19	0.039	0.033
F10b	0.35	12	34	47	20	24	11.09 ± 0.23	0.018	0.042	0.036	11.21 ± 0.25	0.050 ± 0.018	9.85 ± 5.34	0.041	0.036
F11	0.42	15	37	45	17	24	11.22 ± 0.23	0.017	0.040	0.034	11.35 ± 0.25	0.045 ± 0.014	9.11 ± 4.18	0.039	0.033
F12	0.43	18	42	47	18	24	7.34 ± 0.46	0.019	0.044	0.039	7.48 ± 0.35	0.035 ± 0.012	5.33 ± 2.16	0.043	0.038
F13	0.78	17	21	43	11	24	5.68 ± 0.18	0.016	0.037	0.030	5.84 ± 0.18	0.030 ± 0.007	5.67 ± 1.56	0.035	0.028
cont filament[a]	0.80					0.029 ± 0.001	0.016	0.037	0.032		0.032 ± 0.001	0.012 ± 0.002	2.47 ± 0.23	0.030	0.023
mean	0.65	22	32	45	18	24	6.84 ± 0.18	0.020	0.046	0.041	7.03 ± 0.20	0.033 ± 0.009	5.24 ± 1.78	0.045	0.039
median	0.53	16	29	43	17	24	7.32 ± 0.18	0.019	0.045	0.039	7.37 ± 0.21	0.027 ± 0.006	4.64 ± 1.32	0.042	0.037
minimum	0.27	4	14	40	11	24	0.03 ± 0.001	0.015	0.036	0.029	0.03 ± 0.001	0.012 ± 0.002	1.84 ± 0.17	0.030	0.023
maximum	1.37	82	64	65	36	25	11.22 ± 0.46	0.031	0.074	0.071	11.35 ± 0.35	0.081 ± 0.030	10.05 ± 5.74	0.066	0.062

Note. (2) Filament length. (3) Filament mass. (4) Filament mass per unit length. (5) Total critical line-mass. (6) Nonthermal critical line-mass. (7) Thermal critical line-mass. (8)–(11) The amplitude, standard deviation $\sigma = \mathrm{FWHM}/(2\sqrt{2\ln(2)})$, width, and beam-deconvolved width derived from the Gaussian fitting. (12)–(16) The amplitude, flattening radius, density profile, width, and beam-deconvolved width derived from the Plummer fitting.
[a] The amplitude unit is Jy beam^{-1}.

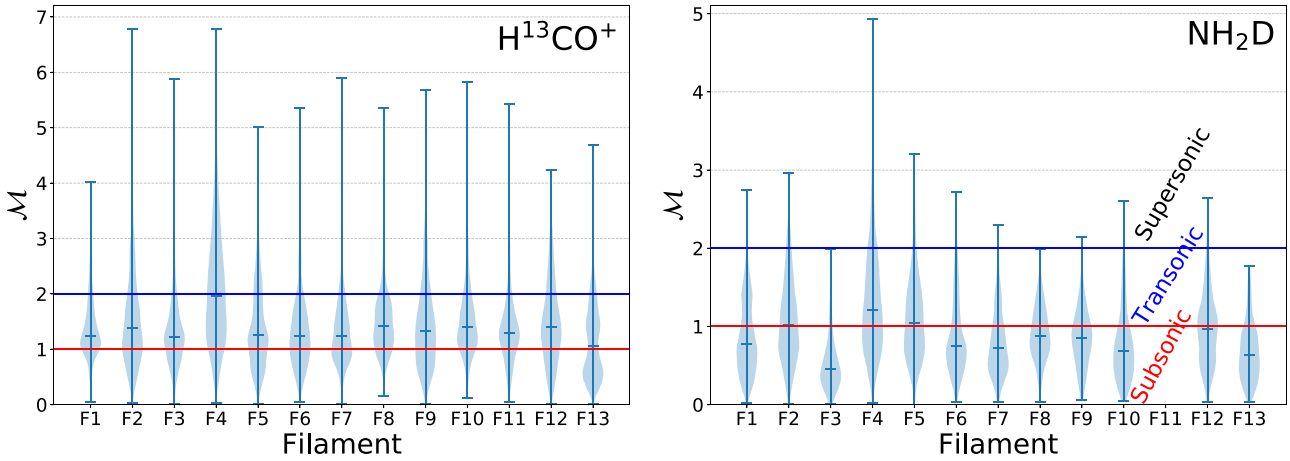

Figure 7. Left and right: violin plots of the Mach number distributions derived from $H^{13}CO^+$ and NH_2D for each filament. The blue bars from top to bottom represent the maximum, mean, and minimum values, respectively. The red and blue solid lines are the Mach numbers of 1 and 2, respectively.

indicates that these filaments contain most of the dense gas (87% = 342/395), as revealed by the total $H^{13}CO^+$ line emission (see Section 4.5 below). The masses per unit length ($M_{\rm line} = M_{\rm fil}/L_{\rm fil}$) of filaments range between 14 and 64 $M_\odot$ pc^{-1}, with a median value of 29 $M_\odot$ pc^{-1} (see Table 1).

The uncertainties in the distance, assumed gas temperature, and variations of the $H^{13}CO^+$ fractional abundance introduce uncertainties in the estimates of the filament masses and masses per unit length. The typical uncertainties in the temperatures derived from NH_3 is ∼15% (see Paper I). The uncertainty in distance from the trigonometric parallax measurement is ∼20% (Chibueze et al. 2014). The standard deviation (std) of $X(H^{13}CO^+)$ for F4 is about 3.7×10^{-11}, which corresponds to a 1σ uncertainty of $70\% = \frac{3.7 \times 10^{-11}}{5.4 \times 10^{-11}}$. We settle on an uncertainty estimate of a factor of ∼2 for both filament mass and mass per unit length according to the propagation of error. Considering of the inclination angle is unknown, the uncertainties in the mass per unit length could be larger.

3.6. Subsonic and Transonic Filaments

The three-dimensional (3D) Mach number is $\mathcal{M} = \sqrt{3}\,\sigma_{\rm nth}/c_{\rm s}$, where $\sigma_{\rm nth} = \sqrt{\sigma^2_{\rm obs} - (\,\triangle_{\rm ch}\,/2\sqrt{2\ln 2})^2 - \sigma^2_{\rm th}}$ is the nonthermal velocity dispersion, $c_{\rm s}$ is the sound speed, and $\triangle_{\rm ch}$ is the channel width. The molecular thermal velocity dispersion can be estimated by $\sigma_{\rm th} = \sqrt{(k_{\rm B}T)/(\mu m_{\rm H})} = 0.098\ {\rm km\ s^{-1}} \left(\frac{T}{\rm K}\right)^{0.5} \mu^{-0.5}$, where $\mu = m/m_{\rm H}$ is the molecular weight, m is the molecular mass, $m_{\rm H}$ is the hydrogen mass, and T is the gas temperature (see also Paper I). The sound speed $c_{\rm s}$ was estimated using a mean molecular weight per free particle of $\mu_{\rm p} = 2.37$ (Kauffmann et al. 2008). Figure 7 shows the Mach number ($\mathcal{M}$) distributions derived from $H^{13}CO^+$ and NH_2D for each filament, except for F11 which has no significant NH_2D detection. Some filaments are partially overlapping, but the corresponding NH_2D line emission shows only one velocity component clearly. This NH_2D emission is assigned to a particular filament based on the minimum velocity differences between NH_2D emission and that filament. The Mach number distributions derived from both $H^{13}CO^+$ and NH_2D lines reveal that the majority of filaments are subsonic ($\mathcal{M} \leqslant 1$) and transonic ($1 < \mathcal{M} \leqslant 2$) in nonthermal motions. In general, the $\mathcal{M}$ derived from NH_2D tends to be smaller than those from $H^{13}CO^+$. This is because NH_2D emission traces colder, denser gas and it is less affected by the protostellar feedback (e.g., outflows) compared to the $H^{13}CO^+$ emission; this is confirmed by the fact that the observed line widths of the former are narrower than those of the latter. The subsonic and transonic features imply a quiescent nature of these filaments. The subsonic and transonic nonthermal line widths found here in dense filaments and dense cores have been seen previously in low-mass star-forming regions (e.g., Perseus, Pineda et al. 2010; Serpens, Gong et al. 2021; Ophiuchus and Taurus, Chen et al. 2019a; L1478 in the California, Chung et al. 2019), and intermediate- and high-mass star-forming regions (e.g., Orion, Hacar et al. 2018; Monsch et al. 2018; Yue et al. 2021; IRDC G035.39–00.33, Sokolov et al. 2018; IRDC G14.225–0.506, Chen et al. 2019b).

4. Discussion

4.1. Continuum Filament

The majority of the continuum emission structures have significant line emission counterparts. One exception is the continuum filamentary structure in the southeastern part of the map (see Figures 1 and 2), which has no line emission counterpart except for a small area near the middle that shows weak emission in the $H^{13}CO^+$, CS, HCN and HCO^+ lines. If this filamentary structure's continuum emission was dominated by free–free or synchrotron emission rather than dust emission, the stellar feedback from O-type stars (O7.5 and O6.5; see Figure 1; Persi & Tapia 2008) on the northeastern side of NGC 6334S are most likely responsible.

We use the `FilFinder` to extract this filamentary structure and its filament spine (see Figure 8). The filament length is about 0.8 pc. Using `Radfil`, the filament widths are about 0.032 and 0.023 pc derived by Gaussian and Plummer fitting based on the continuum emission (Table 1), respectively. The gas mass cannot be reliably estimated because of the unknown fraction of dust emission.

4.2. The Kinematics of Filaments

Figure 6 shows the variations of $v_{\rm LSR}$ and $\sigma_{\rm obs}$ derived from the $H^{13}CO^+$ line emission along the filament. Only one filament (F1) shows monotonic changes along the filament in $v_{\rm LSR}$. By contrast, the $\sigma_{\rm obs}$ shows small fluctuations along F1 rather than a monotonic change. Four continuum cores and two

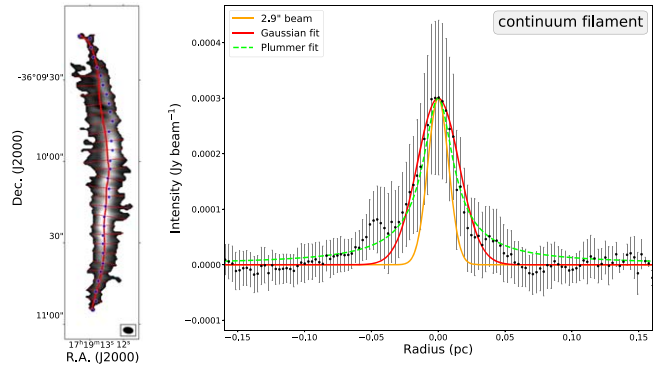

Figure 8. Left: the filament spine (red solid curve) of continuum filament overlaid on the 3 mm continuum image. Right: mean integrated intensity profile (black dots) was built by sampling radial cuts (short red solid lines) every 8 pixels (3.″44 corresponds to ∼0.019 pc at the source distance of 1.3 kpc) along the spine. The radial distance is the projected distance from the peak emission at a given cut (blue dots in the left panel). The error bar represents the standard deviation of the cuts at each radial distance. The orange solid line shows the beam response with an FWHM of ∼2.9.″ The red solid and green dashed lines present the best-fit results of Gaussian and Plummer fitting, respectively.

NH_2D cores are associated with this filament. The core mean σ_{obs} derived from the $H^{13}CO^+$ line is comparable to the σ_{obs} of the filament; however, continuum cores #25 and #21 have slightly larger σ_{obs}. Line widths may be broadened by active star formation. By contrast, some cores show much narrower σ_{obs} than their respective filament; e.g., #31/#36/#49 in F2, #4/#24 in F4, M11 in F5, M10 in F6, and M14 in F10. The measured σ_{obs} of NH_2D is always narrower than those of $H^{13}CO^+$ toward the continuum cores and NH_2D cores, and this feature is also seen in the filaments (see Figure 7). In Section 4.4, we will discuss the properties of σ_{obs} in both continuum cores and NH_2D cores.

Some filaments show only small v_{LSR} variations along their spine (F4b, F5, F7, F8, F10, F10b, and F12), while others display significant variations (F2, F3, F4, F6, F9, F11, and F13). The σ_{obs} also shows irregular variations in all filaments, except for F1 and F13. The latter (F13) shows a roughly increasing trend from east to west (Figure Set 6). There is another gaseous structure seen in the CS (1–0), HCO^+ (1–0), and HCN (1–0) lines, which runs northwest to southeast through the western part of F13. The interaction between two gas flows can broaden the $H^{13}CO^+$ line widths around the intersection regions. That said, the star formation activity is responsible for some of the v_{LSR} and σ_{obs} variations in some filaments. For instance, F4 shows v_{LSR} and σ_{obs} variations at positions in which several strong molecular outflows are detected in the HCN, HCO^+, and CS lines (see Figure 9). These molecular outflows can inject energy and momentum into the immediate surroundings of protostars and affect the gas kinematics, and then the turbulence (or line width) will be increased and the gas velocity will be modified (Li et al. 2019b, 2020b; Lu et al. 2021). Filament F4 encompasses the highest number of continuum cores and YSOs among the filaments (Figures 1 and 6), and therefore the v_{LSR} and σ_{obs} of the $H^{13}CO^+$ line emission in F4 is most likely significantly affected by protostellar feedback. Overall, both protostellar activity and interaction between gas flows can significantly alter the local gas kinematics.

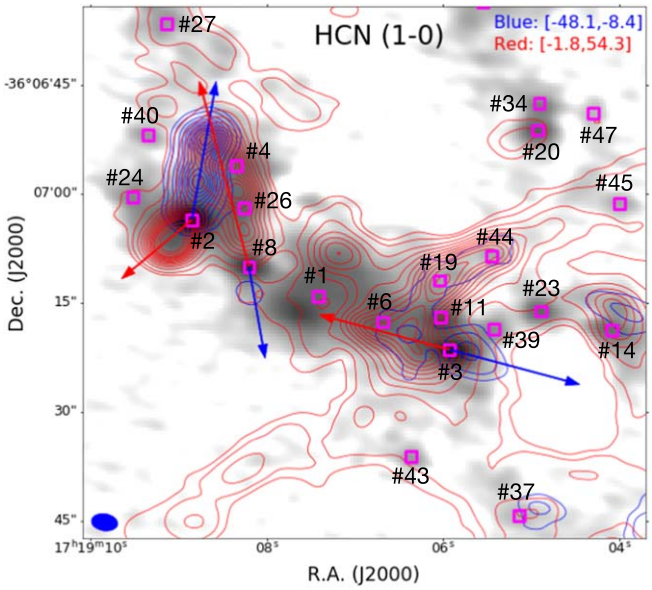

Figure 9. Magenta open squares show the continuum cores. The blueshifted (blue contours) and redshifted (red contours) of HCN (1–0) line emission are overlaid on the continuum image. The arrows show the outflow directions. The beam size is shown in the bottom left.

4.3. Velocity Gradient along F1

As shown in Figure 6, F1 presents a smooth velocity change in $H^{13}CO^+$ emission from the south (-3.3 km s^{-1}) to the north (-1.8 km s^{-1}) along the filament, resulting in a projected velocity gradient of $\sim 1.8 \pm 0.1$ km s^{-1} pc^{-}1. The NH_2D line emission also shows a similar velocity gradient along F1. The velocity gradient along F1 could be attributed to the ongoing accretion flow in F1 (e.g., Kirk et al. 2013), whereas we cannot completely rule out the possibility that the gas kinematics is affected by the external feedback from the western YSOs, such as molecular outflows and/or expanding shells.

If the velocity gradient comes from the accretion flow along the F1 filament, one can estimate the mass flow rate using the derived velocity gradient and filament mass. Assuming that the filament has a cylindrical geometry, the mass flow rate, $\dot{M}$, can be calculated as (see Kirk et al. 2013)

$$\dot{M} = \frac{M \, \nabla_{||} v_{obs}}{\tan(\alpha)} \quad (4)$$

where M is the filament mass, $\nabla_{||} v_{obs}$ is the observed velocity gradient along the filament, and α is the angle of inclination to the plane of sky. Using the derived filament mass of 14 $M_\odot$, the observed velocity gradient of 1.8 km s^{-1} pc^{-1}, and assuming a moderate inclination angle of $\alpha = 45°$, the mass flow rate is estimated to be about 26 $M_\odot$ Myr^{-1} for F1. This result indicates that the F1 filament will double its mass in several freefall times: $\sim 1 \times 10^5$ yr assuming a density of 10^{5-6} cm^{-3} that is the typical value of continuum cores in F1 (see Paper I).

Considering the uncertainties of the derived mass and inclination angle, the estimated flow accretion is roughly comparable to the values of 70 ± 40 $M_\odot$ Myr^{-1} in the IRDC G035.39–00.33 (Henshaw et al. 2014), 17–72 $M_\odot$ Myr^{-1} in the Monoceros R2 (Treviño-Morales et al. 2019), and 20–130 $M_\odot$ Myr^{-1} in the IRDC G14.225–0.506 (Chen et al. 2019b). The estimated mass flow rate could be treated as a

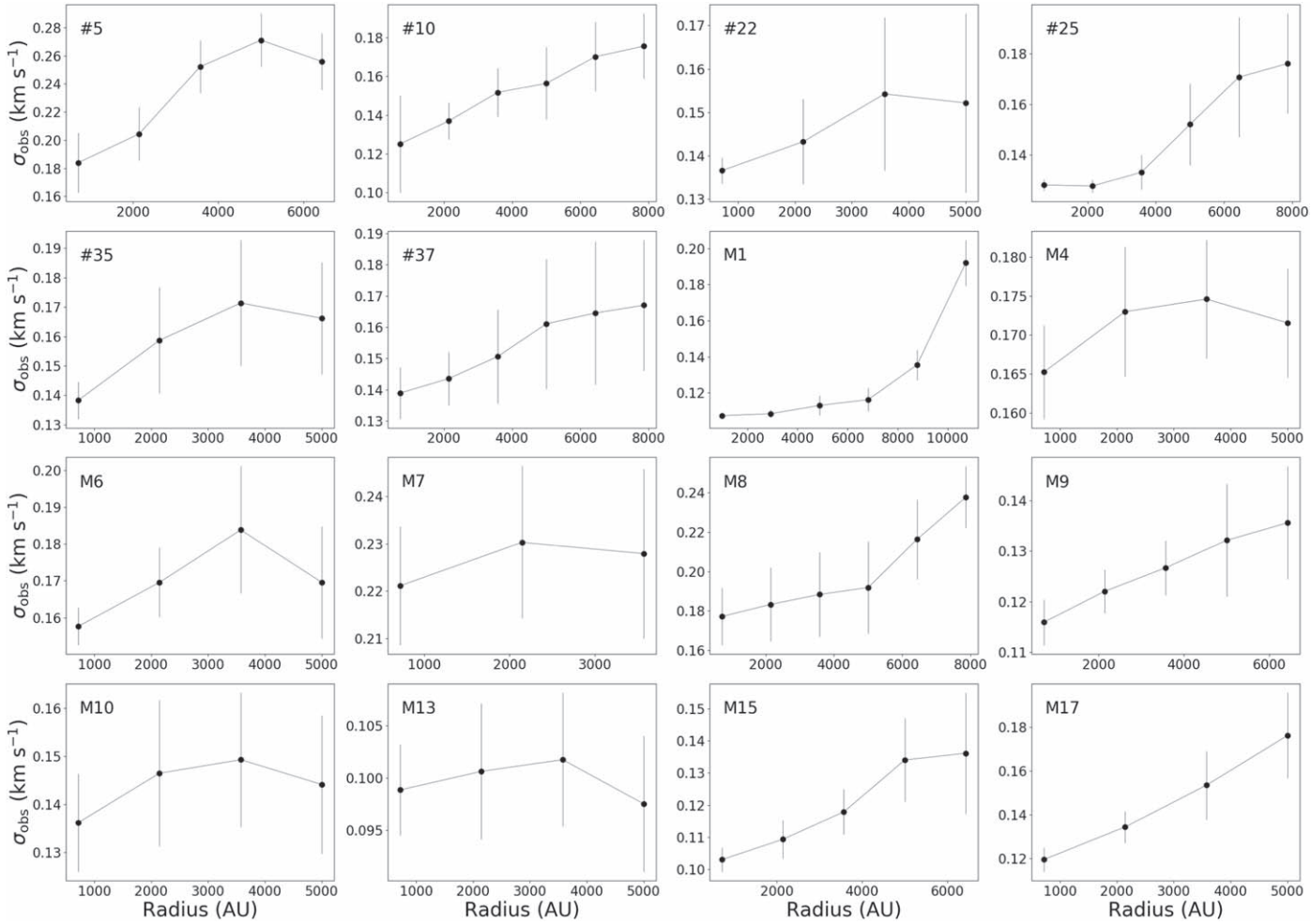

Figure 10. The annularly averaged observed NH_2D velocity dispersions (σ_{obs}) as a function of radial distance from the centers of cores. The error bars show the statistical standard deviation inside each ring divided by the square root of the length of the ring. M1 is modified from Paper II. The name of each core is shown in the top left of each panel.

lower limit, because $H^{13}CO^+$ only traces relatively highly dense gas and the F1 filament is only a small part of a much larger filamentary structure seen in the infrared image (see Figure 1).

A velocity gradient is also detected in sections of the other filaments (e.g., F7 and F13) and around some embedded cores (e.g., #29 in the F3; see Figure 6). Unfortunately, in these cases we cannot distinguish whether the velocity gradient is the result of gas flow or some other physical process, e.g., molecular outflow or rotation. Thus, we refrain from estimating the mass flow rate for other filaments.

4.4. The Kinematics of Embedded Cores

As mentioned in Section 4.3, some cores show smaller σ_{obs} compared to their immediate surroundings. This is probably because the surrounding gas is affected by protostellar activity (e.g., molecular outflows) for some cores. For instance, there is a molecular outflow emanating from #2 in the immediate vicinity of cores #4 and #24, and thus the $H^{13}CO^+$ line widths around both #4 and #24 can be broadened by this outflow activity (see Figure 2). The outflow driven by core #8 also affects the molecular gas around the core #4. The details of molecular outflow analysis is beyond the scope of this paper but is the topic of a follow-up paper.

Furthermore, some of the cores indeed have narrow line widths as revealed by the NH_2D line, which is less affected by the molecular outflows than is $H^{13}CO^+$ as mentioned above. In addition, there are no outflow signatures around these cores. For instance, the observed velocity dispersion appears to decrease toward the center of M1 (see Figure 10). A trend of σ_{obs} decreasing with decreasing radial distance (R_{dist}) from the center of the core is found in 16 cores (see Figure 10), including six continuum cores (#5, #10, #22, #25, #35, and #37) and 10 NH_2D cores (M1, M4, M6, M7, M8, M9, M13, M10, M15, and M17; see also Figure 3 in Paper II for M1). Note that the annularly averaged σ_{obs} has relatively large uncertainties toward the outer edges of the cores due to the low signal-to-noise ratios. The decreasing trend of σ_{obs} toward these core centers may indicate that turbulent dissipation from the filaments to the embedded objects is ongoing, enabling the dense precursors to collapse to form protostars. Alternatively, a number of theoretical studies suggest that for prestellar cores the line width will be smaller in the more central regions if the infall speed decreases toward the center because of an outside-in collapse (e.g., Whitworth & Summers 1985; Lai 2000; Gómez et al. 2021). In summary, some dense cores indeed have a narrower observed velocity dispersion compared to their natal

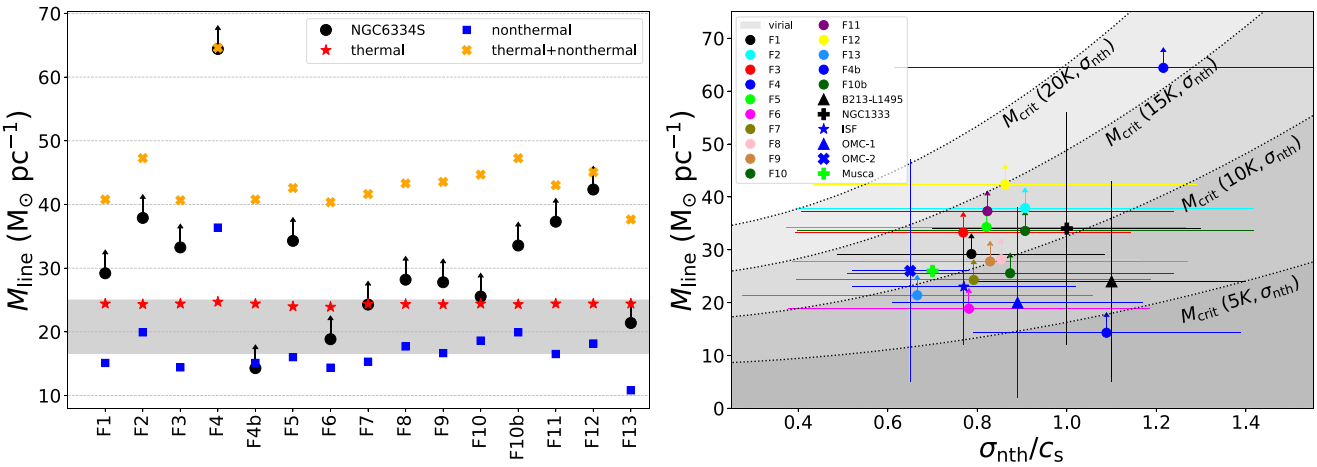

Figure 11. Left: the line-mass for each filament. The black filled circles, red filled stars, blue filled squares, and orange filled crosses show the estimated mass per unit length, thermal critical line-mass, nonthermal critical line-mass, and total (thermal + nonthermal) critical line-mass, respectively. The shaded gray region shows the thermal critical line-mass of 16.6–25 $M_\odot$ pc^{-1} corresponding to the gas temperature of 10–15 K. The arrows indicate that the estimated mass per unit length could be treated as a lower limit. Right: mass per unit length versus $\sigma_{\rm nth}/c_{\rm s}$. The error bars indicate the standard deviations of the parameters. The dashed lines show the expected total critical line-mass for an infinite filament in hydrostatic equilibrium at temperatures of 5 K, 10 K, 15 K, and 20 K, respectively (see Appendix B). The data points of B213-L1495, NGC 1333, ISF, OMC-1, OMC-2, and Musca are retrieved from Hacar et al. (2018).

filaments. This may indicate that turbulent dissipation is taking place in these embedded cores.

4.5. Filament Stability

The comparison between the $M_{\rm line}$ and the corresponding critical line-mass $M_{\rm crit} = 2\sigma_{\rm eff}^2/G$ can be used to evaluate the stability of the filament, where $\sigma_{\rm eff}$ is the effective velocity dispersion and G is the gravitational constant (see Appendix B for the estimation of critical line-mass). Ignoring external pressure and magnetic fields, we compute $M_{\rm crit}$ for filaments assuming they are supported by thermal motions ($\sigma_{\rm eff} = c_{\rm s}$), nonthermal motions ($\sigma_{\rm eff} = \sigma_{\rm nth}$), and total motions (i.e., including both thermal and nonthermal contributions, $\sigma_{\rm eff} = \sqrt{c_{\rm s}^2 + \sigma_{\rm nth}^2}$). As shown in Figure 11, $M_{\rm line}$ is larger than the thermal critical mass ($M_{\rm crit,\ th}$), except for F4b, F6, and F13 that have smaller values than the $M_{\rm crit,\ th}$. This indicates that the filaments would be gravitationally bound (except for F4b, F6, and F13) in the purely thermally supported case. $M_{\rm line}$ is about two times the nonthermal critical mass ($M_{\rm crit,\ nth}$), which suggests that nonthermal support alone cannot prevent gravitational collapse. The ratios of $M_{\rm crit,\ nth}$/$M_{\rm crit,\ th}$ are in the range 0.4–1.4 with a mean value of 0.7, which suggests that the filaments are mostly supported by thermal motions. The estimated $M_{\rm line}$ is smaller than the total critical ($M_{\rm crit,\ tot}$) mass in all of the filaments except for F4.

Although most of the filaments at the current evolutionary state are gravitationally unbound when considering only the balance between self-gravity and the thermal plus nonthermal support, the presence of dense cores suggests that in fact star formation has already started. Note that by neglecting external pressure, magnetic fields, mass uncertainty, and inclination angle uncertainty might bring an addition error into $M_{\rm line}/M_{\rm crit,\ tot}$. Being gravitationally bound is not the sole prerequisite for forming stars in a filament. Fragmentation may have occurred already very early in the evolution of the filaments, if these dense cores originate from filament fragmentation. In addition, the subsonic and transonic dominated filaments and embedded cores indicate that there are low turbulence environments (Paper II); this is analogous to the situation in low-mass star-forming clouds (e.g., Hartmann 2002; Pineda et al. 2010; Hacar & Tafalla 2011; Hacar et al. 2016, 2017). The similarity suggests that similar turbulent conditions may apply in the very early evolutionary phases of low- and high-mass star formation at clump scales (≲a few pc) where turbulence inherited from larger scales (e.g., giant molecular clouds) has already decayed or dissipated in a short time frame (Mac Low 1999; Mac Low & Klessen 2004).

Figure 11 shows $M_{\rm line}$ as a function of $\sigma_{\rm nth}/c_{\rm s}$. The derived masses per unit length are similar to those of narrow filaments in B213-L1495 (24 ± 19 $M_\odot$ pc^{-1}), Musca (26 $M_\odot$ pc^{-1}), NGC 1333 (34 ± 22 $M_\odot$ pc^{-1}), and Orion (23 ± 11 $M_\odot$ pc^{-1} for ISF, 20 ± 18 $M_\odot$ pc^{-1} for OMC-1, and 26 ± 21 $M_\odot$ pc^{-1} for OMC-2; Hacar et al. 2013, 2016, 2017, 2018). The measured $\sigma_{\rm nth}/c_{\rm s}$ are also comparable to those narrow filaments in B213-L1495, Musca, NGC 1333, and Orion (OMC-1/2 and ISF; see Figure 11). These results indicate that the masses per unit length and gas kinematics of narrow filaments in NGC 6334S are comparable to those found in various other environments, from low-mass to high-mass star-forming molecular clouds.

The total gas mass computed from $H^{13}CO^+$ is about 395 $M_\odot$, which is larger than the total gas mass of 160 $M_\odot$ estimated from continuum emission. $H^{13}CO^+$ recovers about 28% of the accumulated mass (1389 $M_\odot$) derived from the H_2 column density map (derived in Paper I; see Appendix A in Paper I for a detailed derivation of the H_2 column density.) This indicates that the extended flux, which contains a significant amount of mass, is not fully recovered by the $H^{13}CO^+$ line toward NGC 6334S in this ALMA observation. The estimated filament masses should thus be treated as lower limits because $H^{13}CO^+$ (1–0; $n_{\rm cr} \sim 10^5$ cm^{-3}) only probes higher density gas components; moreover, the data suffer from missing flux due to the lack of short-spacing observations.

4.6. Population of Embedded Cores and YSOs

The continuum cores are likely at protostellar or prestellar evolutionary phases, while the NH_2D cores seem to be at the starless/prestellar phases (see Paper II). Figure 1(b) shows the distribution of identified dense objects and filaments toward NGC 6334S. The majority of the 45 continuum cores are associated with filaments, while only four continuum cores

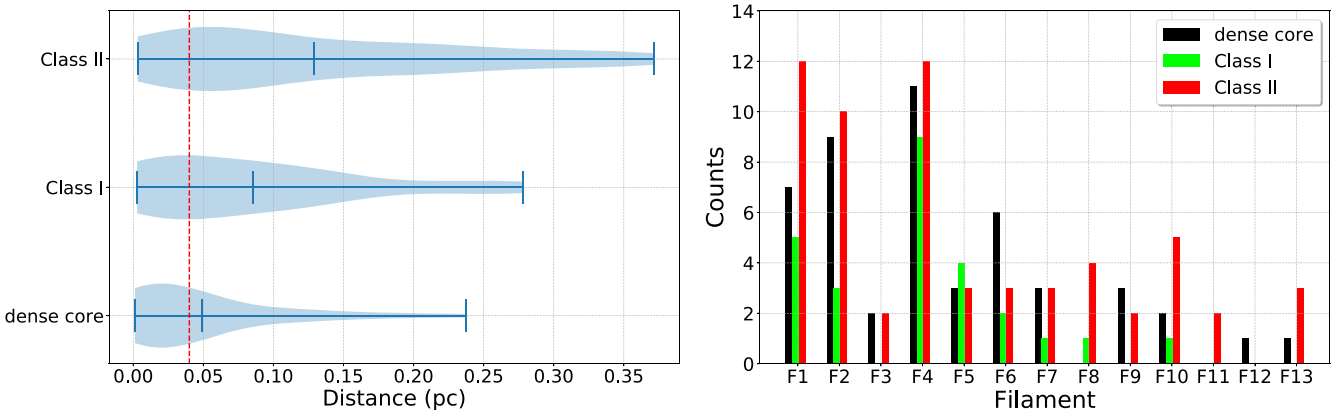

Figure 12. Left: violin plot of the distance distributions for each type object, where the distances are of the objects to the nearest filament spine. The shape of each distribution shows the probability density of the data smoothed by a kernel density estimator. The blue bars from the top to bottom represent the maximum, mean, and minimum values, respectively. The vertical red dashed line is the mean beam-convolved filament width of ∼0.04 pc. Right: the number of the nearest dense cores, and Class I and Class II objects for each filament.

(#22, #28, #33, and #48) are not associated with any identified filament. In addition, 15 out of 17 NH_2D cores are associated with filaments. These results indicate that the majority of dense cores are closely related with filaments in NGC 6334S; as noted earlier, this situation is also found in nearby low-mass star-forming regions (e.g., André et al. 2010).

Figure 1(b) also shows the YSOs' spatial distributions toward NGC 6334S. There are 25 Class I and 58 Class II YSOs in NGC 6334S. The Class I and II YSOs are identified with near-infrared (NEWFIRM) and mid-infrared (IRAC) data (see Willis et al. 2013). Among the 49 identified continuum cores, 12 cores are spatially associated with Class I objects, 5 cores are spatially associated Class II objects, and the remaining 32 cores do not have YSOs counterparts. This indicates that these 32 cores could be younger compared to those cores associated with Class I and Class II YSOs. The majority of YSOs have no continuum core counterparts, perhaps because their continuum emission is too faint ($1\sigma \sim 0.03$ mJy beam^{-1}, or $\sim$0.04 $M_\odot$ at a temperature of 10 K). Furthermore, the YSOs are not associated with NH_2D core counterparts, because the NH_2D line emission is in cold dense gas still in its extremely early evolutionary stages (e.g., starless and/or prestellar).

The majority of continuum cores, NH_2D cores, and Class I objects reside in or close to a filament, while the majority of Class II objects are far away (see Figures 1 and 2). We computed the distance of these objects to their nearest filament spine, in order to search for possible correlations between the evolutionary stages and the distance from the filament. Based on the distance distribution of each type of object shown in Figure 12(a), Class II objects have larger distances than Class I, while Class I objects have larger distances than do the distribution of continuum cores and NH_2D cores. Continuum cores and NH_2D cores are classified as the same type of object in this analysis because the majority of them are embedded in filaments and their evolutionary stages (prestellar or protostellar) are earlier than Class I/II (Paper II). The median distances are 0.09, 0.06, and 0.03 pc for Class II, Class I, and dense cores, respectively. Overall, Figure 12(a) indicates that the more evolved objects are further away from the dense gas filaments in NGC 6334S.

One possible explanation for the different distance distributions is that the evolved objects are moving away from their parental dense filament due to kinematical motions (e.g., slingshot mechanism and ejection; Stutz & Gould 2016; Russeil et al. 2020). Assuming the Class II objects are moving 1 km s^{-1} relative to the filaments (the typical moving velocity of Class II objects in Orion; Stutz & Gould 2016), the estimated moving timescales are between 3×10^3 and 4×10^5 yr, with a median value of 9×10^4 yr. We would like to stress the fact that the actual moving distances may be much smaller than the estimated distances because the YSOs might not necessarily form in the center of the filament. Therefore, the actual dynamical timescales could be smaller than the estimated values. Another possibility is that NGC 6334S has experienced star formation before, and the parental molecular structures of Class II objects have already been moved away from the YSOs (e.g., Vázquez-Semadeni et al. 2017; Kumar et al. 2020) or dispersed/destroyed by star formation feedback. Finally, we cannot rule out the possibility that a few Class II objects may have originated outside of NGC 6334S; especially those objects that are distant from the filaments.

The number of nearest dense cores, and Class I and Class II objects for each filament is presented in Figure 12(b). The number of dense cores and Class I objects around F4 is much higher than for the rest of the filaments, while the number of Class II objects around F1, F2, and F4 is comparable to and higher than that in the other filaments. F4 is located at the central region that encompasses a significant fraction of dense gas and thus it has the potential to form more stars, as evidenced by the numerous continuum cores and YSOs. F2 has the longest physical length in NGC 6334S, and thus it is expected to be associated with more YSOs. As shown in Figure 1, a cluster of YSOs is forming on the western side of F1, resulting in a large number of nearby YSOs. We note that F1 is only a small part of a much larger filamentary structure seen in the infrared image (see Figure 1), implying that it has a large dense gas reservoir from which to form more stars.

In summary, all identified filaments show a narrow width and the majority of them host embedded dense cores. These embedded dense cores are born in environments of low turbulence, which is similar to conditions found in low-mass star-forming regions. More evolved objects are found to be farther away from the filaments, suggesting YSOs or filaments have a tendency to move away from their natal place as they evolve.

5. Conclusion

In this paper, we investigated the velocity-coherent filaments in the massive IRDC NGC 6334S using ALMA observations.

Using the $H^{13}CO^+$ (1–0) line emission, we have identified 13 velocity-coherent filaments. We investigated the physical properties of the identified filaments and characterized the dense objects in NGC 6334S. Our main findings are summarized as follows:

1. The filaments show a compact radial distribution with a median $FWHM_{decon}$ of ∼0.04 pc. The derived filament widths are narrower than the previously proposed "quasi-universal" 0.1 pc filament width. In addition, the filament widths are roughly twice the size of embedded cores (radius ∼ 0.017 pc). The higher spatial resolution observations and higher density gas tracer tend to identify even narrower and lower mass filaments.
2. The nonthermal motions are predominantly subsonic and transonic in all observed filaments; the single exception is F4, which has been significantly affected by protostellar feedback. The filaments are largely supported by thermal motions. The physical properties (mass, mass per unit length, gas kinematics, and width) of filaments are similar to those seen in narrow filaments found in various environments such as low-mass, intermediate-mass, and high-mass star-forming regions (i.e., B213-L1495, Musca, NGC 1333, Orion, and G035.39–00.33).
3. A fraction of the embedded objects show narrower observed velocity dispersions (σ_{obs}) than their natal filaments, which may indicate that turbulent dissipation is taking place in these embedded cores. The subsonic and transonic dominated filaments and dense cores indicate that in NGC 6334S the stars are often born in environments of low turbulent motions. This conclusion hints that similar small turbulent conditions exist at very early evolutionary stages of low- and high-mass star formation at clump scales.
4. The median distance to the nearest filament for dense cores, and Class I and Class II objects, is 0.03 pc, 0.06 pc, and 0.09 pc, respectively. The increasing distances suggest that the more evolved objects are farther away from the filaments in NGC 6334S, perhaps because either YSOs or filaments tend to move away from their natal place as they evolve.

We thank the anonymous referee for the constructive report. D.L. acknowledges the support from the National Natural Science Foundation of China grant No. 11988101. J.W. and K. Q. acknowledge the support from the National Key R&D Program of China (No. 2017YFA0402604) and the Natural Science Foundation of China under grants U1731237. C.W.L. is supported by the Basic Science Research Program through the National Research Foundation of Korea (NRF) funded by the Ministry of Education, Science and Technology (NRF-2019R1A2C1010851). P.S. was partially supported by a Grant-in-Aid for Scientific Research (KAKENHI Number 18H01259) of the Japan Society for the Promotion of Science (JSPS). H.B. acknowledges support from the Deutsche Forschungsgemeinschaft (DFG, German Research Foundation) Project-ID 138713538 SFB 881 ("The Milky Way System," subproject B1). H.B. further acknowledges funding from the European Research Council under the Horizon 2020 Framework Program via the ERC Consolidator grant CSF-648505. J.M.G. acknowledges the support of the grants AYA2017-84390-C2-R and PID2020-117710GB-I00 (AEI/FEDER, UE). A.P. acknowledges financial support from the UNAM-PAPIIT IN111421 grant, the Sistema Nacional de Investigadores of CONACyT, and from the CONACyT project number 86372 of the "Ciencia de Frontera 2019" program, entitled 'Citlalcóatl: A multiscale study at the new frontier of the formation and early evolution of stars and planetary systems,' México. H.L.L. is supported by National Natural Science Foundation of China (NSFC) through the grant No.12103045. I.J.-S. has received partial support from the Spanish State Research Agency (AEI) project number PID2019-105552RB-C41. This paper makes use of the following ALMA data: ADS/JAO.ALMA#2016.1.00951.S. ALMA is a partnership of ESO (representing its member states), NSF(USA), and NINS (Japan), together with NRC (Canada) and NSC and ASIAA (Taiwan) and KASI (Republic of Korea), in cooperation with the Republic of Chile. The Joint ALMA Observatory is operated by ESO, AUI/NRAO and NAOJ.

Facilities: ALMA, Herschel.

Software: CASA (McMullin et al. 2007), APLpy (Robitaille & Bressert 2012), Matplotlib (Hunter 2007), Astropy (Astropy Collaboration et al. 2013), PySpecKit (Ginsburg & Mirocha 2011), Numpy (Harris et al. 2020).

Appendix A
Column Density

Assuming local LTE, the column density of molecules can be calculated following Mangum & Shirley (2015):

$$N = C_\tau \frac{3h}{8\pi^3 R} \frac{Q_{\rm rot}}{S\mu^2 g_{\rm u}} \frac{\exp\left(\frac{E_{\rm u}}{kT_{\rm ex}}\right)}{\exp\left(\frac{h\nu}{kT_{\rm ex}}\right) - 1} \times (J_\nu(T_{\rm ex}) - J_\nu(T_{\rm bg}))^{-1} \int \frac{T_{\rm R}\, dv}{f}, \quad \text{(A1)}$$

where $C_\tau = \tau/(1 - \exp(-\tau))$ is the optical depth correction factor, h is the Planck constant, $S\mu^2$ is the line strength multiplied by the square of the dipole moment, R is the line intensity, $g_{\rm u}$ is the statistical weight of the upper level, $T_{\rm ex}$ is the excitation temperature, $T_{\rm bg}$ is the background temperature, $E_{\rm u}$ is the energy of the upper state, ν is the transition frequency, $\int T_{\rm R} dv$ is the velocity-integrated intensity, f is the filling factor, and $Q_{\rm rot}$ is the partition function. Here, f is assumed to be 1 and the $T_{\rm NH_3}$ approximates the $T_{\rm ex}$ of molecular lines (see Section 3.1). Both $H^{13}CO^+$ and NH_2D emission are generally optically thin. The NH_2D partition function is $Q_{\rm rot} = 0.73 T_{\rm ex}^{3/2} + 6.56$, which is the best-fit result from a fit to the partition function obtained from the CDMS catalogs at the different excitation temperatures of 10–300 K (Müller et al. 2005), while the $H^{13}CO^+$ partition function can be estimated from $Q_{\rm rot} \approx kT_{\rm ex}/hB + 1/3$, which is an approximation for diatomic linear molecules (Mangum & Shirley 2015). For NH_2D, the molecular parameters are 15 for $g_{\rm u}$, 11.91 D for $S\mu^2$, 20.68 K for $E_{\rm u}$, 85.926 GHz for ν, and 1/2 for R, which is the relative intensity of the main hyperfine transition with respect to the other hyperfine transitions. For $H^{13}CO^+$, the molecular parameters are 3 for $g_{\rm u}$, 15.21 D^2 for $S\mu^2$, 15.21 K for $E_{\rm u}/k$, 86.754288 GHz for ν, and 1 for R.

$N_{\rm H_2}$ is derived from the continuum emission with

$$N_{\rm H_2} = \eta \frac{S_\nu}{\Omega\, B_\nu(T_{\rm dust})\, \kappa_\nu\, \mu\, m_{\rm H}}, \quad \text{(A2)}$$

where $\eta = 100$ is the gas-to-dust ratio, S_ν is the peak flux density, Ω is the beam solid angle, $m_{\rm H}$ is the proton mass, $\mu = 2.8$ is the mean molecular weight of the ISM (Kauffmann et al. 2008), and κ_ν is the dust opacity at a frequency of ν. We use $\kappa_\nu = 0.235\,{\rm cm^{-2}\ g^{-1}}$ by assuming $\kappa_\nu = 10(\nu/1.2{\rm THz})^\beta\,{\rm cm^{-2}\ g^{-1}}$ and $\beta = 1.5$ (Hildebrand 1983).

Appendix B
Filament Critical Line-mass

Assuming the filament is an infinite self-gravitating isothermal cylinder in hydrostatic equilibrium, the critical line-mass of the filament can be estimated by (Ostriker 1964):

$$M_{\rm crit} = \frac{2\sigma_{\rm eff}^2}{G}, \tag{B1}$$

where $\sigma_{\rm eff}$ is the effective velocity dispersion and G is the gravitational constant. If the thermal gas pressure is the only force opposing gravity, then $\sigma_{\rm eff} = c_{\rm s}$. If turbulence is the only force against gravity, $\sigma_{\rm eff} = \sigma_{\rm nth}$. If both thermal and turbulence supports are considered, $\sigma_{\rm eff} = \sqrt{\sigma_{\rm nth}^2 + c_{\rm s}^2}$. In the last case, Equation (B1) can be written as (see also Hacar et al. 2018):

$$M_{\rm crit}(T,\,\sigma_{\rm nth}) = \frac{2\,c_{\rm s}^2}{G}\left(1 + \left(\frac{\sigma_{\rm nth}}{c_{\rm s}}\right)^2\right). \tag{B2}$$

ORCID iDs

Shanghuo Li https://orcid.org/0000-0003-1275-5251
Patricio Sanhueza https://orcid.org/0000-0002-7125-7685
Chang Won Lee https://orcid.org/0000-0002-3179-6334
Qizhou Zhang https://orcid.org/0000-0003-2384-6589
Henrik Beuther https://orcid.org/0000-0002-1700-090X
Aina Palau https://orcid.org/0000-0002-9569-9234
Hong-Li Liu https://orcid.org/0000-0003-3343-9645
Hauyu Baobab Liu https://orcid.org/0000-0003-2300-2626
Izaskun Jiménez-Serra https://orcid.org/0000-0003-4493-8714
Kee-Tae Kim https://orcid.org/0000-0003-2412-7092
Siyi Feng https://orcid.org/0000-0002-4707-8409
Tie Liu https://orcid.org/0000-0002-5286-2564
Junzhi Wang https://orcid.org/0000-0001-6106-1171
Di Li https://orcid.org/0000-0003-3010-7661
Keping Qiu https://orcid.org/0000-0002-5093-5088
Xing Lu https://orcid.org/0000-0003-2619-9305
Josep Miquel Girart https://orcid.org/0000-0002-3829-5591
Ke Wang https://orcid.org/0000-0002-7237-3856
Fei Li https://orcid.org/0000-0002-9832-8295
Juan Li https://orcid.org/0000-0003-3520-6191
Yue Cao https://orcid.org/0000-0002-6368-7570
Shinyoung Kim https://orcid.org/0000-0001-9333-5608

References

André, P., Di Francesco, J., Ward-Thompson, D., et al. 2014, in Protostars and Planets VI, ed. H. Beuther et al. (Tuscon, AZ: Univ. Arizona Press), 27
André, P., Men'shchikov, A., Bontemps, S., et al. 2010, A&A, 518, L102
Arzoumanian, D., André, P., Didelon, P., et al. 2011, A&A, 529, L6
Arzoumanian, D., André, P., Könyves, V., et al. 2019, A&A, 621, A42
Astropy Collaboration, Robitaille, T. P., Tollerud, E. J., et al. 2013, A&A, 558, A33
Beuther, H., Ragan, S. E., Johnston, K., et al. 2015, A&A, 584, A67
Busquet, G., Estalella, R., Palau, A., et al. 2016, ApJ, 819, 139
Butner, H. M., Lada, E. A., & Loren, R. B. 1995, ApJ, 448, 207
Chen, C.-Y., Mundy, L. G., Ostriker, E. C., Storm, S., & Dhabal, A. 2020, MNRAS, 494, 3675
Chen, H. H.-H., Pineda, J. E., Goodman, A. A., et al. 2019a, ApJ, 877, 93
Chen, H.-R. V., Zhang, Q., Wright, M. C. H., et al. 2019b, ApJ, 875, 24
Chibueze, J. O., Omodaka, T., Handa, T., et al. 2014, ApJ, 784, 114
Chung, E. J., Lee, C. W., Kim, S., et al. 2019, ApJ, 877, 114
Churchwell, E., Babler, B. L., Meade, M. R., et al. 2009, PASP, 121, 213
Clarke, S. D., Whitworth, A. P., Duarte-Cabral, A., & Hubber, D. A. 2017, MNRAS, 468, 2489
Contreras, Y., Garay, G., Rathborne, J. M., & Sanhueza, P. 2016, MNRAS, 456, 2041
Contreras, Y., Sanhueza, P., Jackson, J. M., et al. 2018, ApJ, 861, 14
Cox, N. L. J., Arzoumanian, D., André, P., et al. 2016, A&A, 590, A110
Gerner, T., Beuther, H., Semenov, D., et al. 2014, A&A, 563, A97
Ginsburg, A., & Mirocha, J. 2011, PySpecKit: Python Spectroscopic Toolkit, Astrophysics Source Code Library, ascl:1109.001
Gómez, G. C., & Vázquez-Semadeni, E. 2014, ApJ, 791, 124
Gómez, G. C., Vázquez-Semadeni, E., & Palau, A. 2021, MNRAS, 502, 4963
Gong, H., & Ostriker, E. C. 2011, ApJ, 729, 120
Gong, Y., Belloche, A., Du, F. J., et al. 2021, A&A, 646, A170
Goodman, A. A., Alves, J., Beaumont, C. N., et al. 2014, ApJ, 797, 53
Hacar, A., Kainulainen, J., Tafalla, M., Beuther, H., & Alves, J. 2016, A&A, 587, A97
Hacar, A., & Tafalla, M. 2011, A&A, 533, A34
Hacar, A., Tafalla, M., & Alves, J. 2017, A&A, 606, A123
Hacar, A., Tafalla, M., Forbrich, J., et al. 2018, A&A, 610, A77
Hacar, A., Tafalla, M., Kauffmann, J., & Kovács, A. 2013, A&A, 554, A55
Harris, C. R., Millman, K. J., van der Walt, S. J., et al. 2020, Natur, 585, 357
Hartmann, L. 2002, ApJ, 578, 914
Hartmann, L., & Burkert, A. 2007, ApJ, 654, 988
Heitsch, F., Ballesteros-Paredes, J., & Hartmann, L. 2009, ApJ, 704, 1735
Heitsch, F., Hartmann, L. W., Slyz, A. D., Devriendt, J. E. G., & Burkert, A. 2008, ApJ, 674, 316
Hennebelle, P. 2013, A&A, 556, A153
Henshaw, J. D., Caselli, P., Fontani, F., Jiménez-Serra, I., & Tan, J. C. 2014, MNRAS, 440, 2860
Henshaw, J. D., Jiménez-Serra, I., Longmore, S. N., et al. 2017, MNRAS, 464, L31
Hildebrand, R. H. 1983, QJRAS, 24, 267
Hoq, S., Jackson, J. M., Foster, J. B., et al. 2013, ApJ, 777, 157
Huchra, J. P., & Geller, M. J. 1982, ApJ, 257, 423
Hunter, J. D. 2007, CSE, 9, 90
Inutsuka, S.-I., & Miyama, S. M. 1992, ApJ, 388, 392
Jiménez-Serra, I., Caselli, P., Fontani, F., et al. 2014, MNRAS, 439, 1996
Kainulainen, J., Hacar, A., Alves, J., et al. 2016, A&A, 586, A27
Kauffmann, J., Bertoldi, F., Bourke, T. L., Evans, N. J. I., & Lee, C. W. 2008, A&A, 487, 993
Kirk, H., Myers, P. C., Bourke, T. L., et al. 2013, ApJ, 766, 115
Könyves, V., André, P., Men'shchikov, A., et al. 2015, A&A, 584, A91
Kumar, M. S. N., Palmeirim, P., Arzoumanian, D., & Inutsuka, S. I. 2020, A&A, 642, A87
Lai, D. 2000, ApJ, 540, 946
Li, D., & Goldsmith, P. F. 2012, ApJ, 756, 12
Li, G.-X., Urquhart, J. S., Leurini, S., et al. 2016, A&A, 591, A5
Li, S., Lu, X., Zhang, Q., et al. 2021, ApJL, 912, L7
Li, S., Sanhueza, P., Zhang, Q., et al. 2020b, ApJ, 903, 119
Li, S., Wang, J., Fang, M., et al. 2019b, ApJ, 878, 29
Li, S., Zhang, Q., Liu, H. B., et al. 2020a, ApJ, 896, 110
Li, S., Zhang, Q., Pillai, T., et al. 2019a, ApJ, 886, 130
Lin, Y., Liu, H. B., Dale, J. E., et al. 2017, ApJ, 840, 22
Liu, H. B., Jiménez-Serra, I., Ho, P. T. P., et al. 2012, ApJ, 756, 10
Liu, H.-L., Stutz, A., & Yuan, J.-H. 2018, MNRAS, 478, 2119
Liu, H.-L., Stutz, A., & Yuan, J.-H. 2019, MNRAS, 487, 1259
Lu, X., Li, S., Ginsburg, A., et al. 2021, ApJ, 909, 177
Lu, X., Zhang, Q., Liu, H. B., et al. 2018, ApJ, 855, 9
Mac Low, M.-M. 1999, ApJ, 524, 169
Mac Low, M.-M., & Klessen, R. S. 2004, RvMP, 76, 125
Mangum, J. G., & Shirley, Y. L. 2015, PASP, 127, 266
McBreen, B., Fazio, G. G., Stier, M., & Wright, E. L. 1979, ApJL, 232, L183
McMullin, J. P., Waters, B., Schiebel, D., Young, W., & Golap, K. 2007, in ASP Conf. Ser. 376, Astronomical Data Analysis Software and Systems XVI, ed. R. A. Shaw, F. Hill, & D. J. Bell (San Francisco, CA: ASP), 127
Men'shchikov, A., André, P., Didelon, P., et al. 2010, A&A, 518, L103
Miville-Deschênes, M. A., Martin, P. G., Abergel, A., et al. 2010, A&A, 518, L104

Miyama, S. M., Narita, S., & Hayashi, C. 1987, PThPh, 78, 1051
Molinari, S., Swinyard, B., Bally, J., et al. 2010, A&A, 518, L100
Monsch, K., Pineda, J. E., Liu, H. B., et al. 2018, ApJ, 861, 77
Morii, K., Sanhueza, P., Nakamura, F., et al. 2021, ApJ, 923, 147
Müller, H. S. P., Schlöder, F., Stutzki, J., & Winnewisser, G. 2005, JMoSt, 742, 215
Myers, P. C. 2009, ApJ, 700, 1609
Nagai, T., Inutsuka, S.-i., & Miyama, S. M. 1998, ApJ, 506, 306
Nakamura, F., & Li, Z.-Y. 2008, ApJ, 687, 354
Nutter, D., Kirk, J. M., Stamatellos, D., & Ward-Thompson, D. 2008, MNRAS, 384, 755
Ostriker, J. 1964, ApJ, 140, 1056
Padoan, P., Juvela, M., Goodman, A. A., & Nordlund, Å. 2001, ApJ, 553, 227
Padoan, P., Nordlund, Å., Kritsuk, A. G., Norman, M. L., & Li, P. S. 2007, ApJ, 661, 972
Palmeirim, P., André, P., Kirk, J., et al. 2013, A&A, 550, A38
Peretto, N., Fuller, G. A., André, P., et al. 2014, A&A, 561, A83
Persi, P., & Tapia, M. 2008, in Star Formation in NGC 6334, ed. B. Reipurth, Vol. 5 (San Francisco, CA: ASP), 456
Pineda, J. E., Goodman, A. A., Arce, H. G., et al. 2010, ApJL, 712, L116
Robitaille, T., & Bressert, E. 2012, APLpy: Astronomical Plotting Library in Python, Astrophysics Source Code Library, ascl:1208.017
Russeil, D., Schneider, N., Anderson, L. D., et al. 2013, A&A, 554, A42
Russeil, D., Zavagno, A., Nguyen, A., et al. 2020, A&A, 642, A21
Sanhueza, P., Contreras, Y., Wu, B., et al. 2019, ApJ, 886, 102
Sanhueza, P., Girart, J. M., Padovani, M., et al. 2021, ApJL, 915, L10
Sanhueza, P., Jackson, J. M., Foster, J. B., et al. 2012, ApJ, 756, 60
Sanhueza, P., Jackson, J. M., Foster, J. B., et al. 2013, ApJ, 773, 123
Sanhueza, P., Jackson, J. M., Zhang, Q., et al. 2017, ApJ, 841, 97
Sepúlveda, I., Estalella, R., Anglada, G., et al. 2020, A&A, 644, A128
Smith, R. J., Glover, S. C. O., & Klessen, R. S. 2014, MNRAS, 445, 2900
Sokolov, V., Wang, K., Pineda, J. E., et al. 2018, A&A, 611, L3
Soler, J. D., Beuther, H., Syed, J., et al. 2020, A&A, 642, A163
Stutz, A. M., & Gould, A. 2016, A&A, 590, A2
Tan, J. C., Kong, S., Butler, M. J., Caselli, P., & Fontani, F. 2013, ApJ, 779, 96
Treviño-Morales, S. P., Fuente, A., Sánchez-Monge, Á., et al. 2019, A&A, 629, A81
Van Loo, S., Keto, E., & Zhang, Q. 2014, ApJ, 789, 37
Vázquez-Semadeni, E., González-Samaniego, A., & Colín, P. 2017, MNRAS, 467, 1313
Wang, K., Testi, L., Ginsburg, A., et al. 2015, MNRAS, 450, 4043
Wang, K., Zhang, Q., Testi, L., et al. 2014, MNRAS, 439, 3275
Wang, Y., Beuther, H., Schneider, N., et al. 2020, A&A, 641, A53
Whitworth, A., & Summers, D. 1985, MNRAS, 214, 1
Willis, S., Marengo, M., Allen, L., et al. 2013, ApJ, 778, 96
Yuan, J., Li, J.-Z., Wu, Y., et al. 2018, ApJ, 852, 12
Yue, N.-N., Li, D., Zhang, Q.-Z., et al. 2021, RAA, 21, 024
Zhang, Q., Wang, Y., Pillai, T., & Rathborne, J. 2009, ApJ, 696, 268
Zucker, C., Battersby, C., & Goodman, A. 2015, ApJ, 815, 23
Zucker, C., & Chen, H. H.-H. 2018, ApJ, 864, 152